

Journal of Geophysical Research: Oceans

RESEARCH ARTICLE

10.1002/2016JC012646

Special Section:

The Southern Ocean Carbon and Climate Observations and Modeling (SOCCOM) Project: Technologies, Methods, and Early Results

Key Points:

- The carbon budget in the Southern Ocean is analyzed using a physical-biogeochemical state estimate for the years 2008–2012
- The dissolved inorganic carbon budget is dominated by variability in the overturning circulation
- Temporal variability is enhanced near topography and fronts

Supporting Information:

- Supporting Information S1
- Figure S1

Correspondence to:

I. Rosso,
irocco@ucsd.edu

Citation:

Rosso, I., M. R. Mazloff, A. Verdy, and L. D. Talley (2017), Space and time variability of the Southern Ocean carbon budget, *J. Geophys. Res. Oceans*, 122, 7407–7432, doi:10.1002/2016JC012646.

Received 3 JAN 2017

Accepted 1 AUG 2017

Accepted article online 11 AUG 2017

Published online 14 SEP 2017

Space and time variability of the Southern Ocean carbon budget

Isabella Rosso¹ , Matthew R. Mazloff¹ , Ariane Verdy¹ , and Lynne D. Talley¹ 

¹Scripps Institution of Oceanography, University of California San Diego, La Jolla, California, USA

Abstract The upper ocean dissolved inorganic carbon (DIC) concentration is regulated by advective and diffusive transport divergence, biological processes, freshwater, and air-sea CO₂ fluxes. The relative importance of these mechanisms in the Southern Ocean is uncertain, as year-round observations in this area have been limited. We use a novel physical-biogeochemical state estimate of the Southern Ocean to construct a closed DIC budget of the top 650 m and investigate the spatial and temporal variability of the different components of the carbon system. The dominant mechanisms of variability in upper ocean DIC depend on location and time and space scales considered. Advective transport is the most influential mechanism and governs the local DIC budget across the 10 day–5 year timescales analyzed. Diffusive effects are nearly negligible. The large-scale transport structure is primarily set by upwelling and downwelling, though both the lateral ageostrophic and geostrophic transports are significant. In the Antarctic Circumpolar Current, the carbon budget components are also influenced by the presence of topography and biological hot spots. In the subtropics, evaporation and air-sea CO₂ flux primarily balances the sink due to biological production and advective transport. Finally, in the subpolar region sea ice processes, which change the seawater volume and thus the DIC concentration, compensate the large impact of the advective transport and modulate the timing of biological activity and air-sea CO₂ flux.

1. Introduction

The Southern Ocean contributes importantly to the global climate system through the upwelling of deep, centuries-old water that is rich in carbon and nutrients [Morrison *et al.*, 2015; Talley, 2013]. These deep waters are then transformed by exchange with the atmosphere and the upper and intermediate waters, and eventually sink again [Marshall and Speer, 2012; Talley, 2013], transporting dissolved gases with them. This work focuses on the cycle of dissolved inorganic carbon (DIC). DIC is of particular importance because it is directly linked to atmospheric CO₂ concentrations. The DIC distribution is set by physical and biological processes as well as air-sea flux of CO₂, as outlined in the next few paragraphs.

The physical processes of advection and diffusion transport and mix DIC between ocean basins, across fronts, and between the surface and the abyss, affecting its spatial and temporal variability. From the wind-driven large-scale circulation to the energetic submesoscale eddies, the ocean circulation modulates the exchange of carbon laterally and vertically within the ocean and exchanges with the atmosphere [e.g., Bakker *et al.*, 1997; Boyd *et al.*, 2000; Ito *et al.*, 2004; Lovenduski *et al.*, 2008; Resplandy *et al.*, 2014].

The biological mechanisms of photosynthesis and remineralization impact the DIC concentration [Unkovich *et al.*, 2013]. Biological productivity draws DIC down and is limited by light and the availability of nutrients and trace metals including iron [Martin, 1990]. Productivity in the Southern Ocean is exceptionally large where the limitation of iron is not active [e.g., Blain *et al.*, 2007]. Iron can be supplied by dust deposition [Mahowald *et al.*, 2005], mixing [e.g., Park *et al.*, 2008], stirring [e.g., Abraham *et al.*, 2000], entrainment of the mixed-layer depth [Carranza and Gille, 2015], wind-driven upwelling [Gille *et al.*, 2014], and meso- and submesoscale vertical processes [e.g., Boyd *et al.*, 2000; Coale *et al.*, 2004; Blain *et al.*, 2007; Rosso *et al.*, 2016]. Locations of enhanced biological activity, due to nutrient and iron enhancement, are found along the Polar Front [Moore and Abbott, 2000], close to islands and larger topographic features including the Crozet Islands [e.g., Planquette *et al.*, 2007] and the Kerguelen Plateau [e.g., Chever *et al.*, 2010; Bowie *et al.*, 2015; Gille *et al.*, 2014], and in Antarctic waters including the Weddell and Scotia Seas [e.g., de Baar *et al.*, 1990] and the Ross Sea [e.g., Arrigo and van Dijken, 2004].

The DIC concentration budget is also physically affected by changes in seawater volume due to freshwater flux, because concentration is mass per unit volume. The freshwater flux arises from precipitation, evaporation, sea ice growth and melt, glacial runoff, and river input. These processes can be particularly large in the subtropics, due to high evaporation [Talley, 2008], in the Antarctic Circumpolar Current (ACC) due to net precipitation [e.g., Cerovečki *et al.*, 2013], and in the sea ice zone where ice transport redistributes freshwater [Abernathay *et al.*, 2016].

Carbon dioxide exchange between the ocean and atmosphere, which directly affects DIC, is of fundamental interest because of its capacity to control the changing climate. air-sea exchange is governed by solubility, water temperature, gas transfer velocity, and the partial pressure gradient of CO₂ between seawater and air [e.g., Wanninkhof, 1992]. This exchange drives a net global annual oceanic uptake of anthropogenic carbon estimated to be about 2 Pg C yr⁻¹ [e.g., Takahashi *et al.*, 2009; Mikaloff Fletcher *et al.*, 2006; Khatiwala *et al.*, 2009; Wanninkhof *et al.*, 2013]. Observational inferences suggest that the Southern Ocean is responsible for absorbing half of this global annual uptake [e.g., Takahashi *et al.*, 2012]. However, there are large uncertainties associated with the estimates of carbon flux, especially in the Southern Ocean [e.g., Mikaloff Fletcher *et al.*, 2006; Gruber *et al.*, 2009; Le Quéré *et al.*, 2009; Fay *et al.*, 2014; Landschützer *et al.*, 2014; Munro *et al.*, 2015]. These uncertainties derive from the accuracy of measurements of wind speed and the parameterization of the gas transfer rate [e.g., Signorini and McClain, 2009], observational uncertainty, and uncertainty associated with mapping methods [e.g., Mikaloff Fletcher *et al.*, 2006; Takahashi *et al.*, 2002].

Reducing the uncertainties by increasing data coverage is extremely important, as the air-sea CO₂ flux and the ocean carbon concentration are known to have large spatial and temporal variability, from seasonal to multidecadal scales [e.g., Takahashi *et al.*, 2009; Lenton *et al.*, 2012; Resplandy *et al.*, 2014; Landschützer *et al.*, 2014, 2015; Resplandy *et al.*, 2015]. Despite the growing dataset of in situ observations of carbon and nutrients [Bakker, 2014, 2016; Key *et al.*, 2015; Olsen *et al.*, 2016], observing the Southern Ocean is still temporally and spatially limited due to its rough conditions and remoteness [Takahashi *et al.*, 2009]. The Southern Ocean Carbon and Climate Observations and Modeling (SOCCOM) project is greatly expanding the observational coverage in space and time, by deploying an array of autonomous floats equipped with temperature, salinity, and biogeochemical sensors, and using relationships between the properties to derive the components of the carbon system [Williams *et al.*, 2017].

Closing the Southern Ocean carbon budget using observations alone is therefore very challenging. To pull together these many, yet still sparse, observations of the Southern Ocean carbon system, we use state estimation, which combines these observations with an ocean model. Incorporation of a model reveals the locations and drivers of maximum variability, across multiple temporal and spatial scales, and in the multiple physical and biogeochemical regimes that make up the Southern Ocean. This is a crucial step if we want to improve our understanding of the role of the Southern Ocean in the evolving global climate system. We use the novel Biogeochemical Southern Ocean State Estimate (B-SOSE) [Verdy and Mazloff, 2017], a data-assimilating model solution at 1/3° resolution. B-SOSE is an integral part of SOCCOM, designed to connect observations with unconstrained models, particularly for biogeochemical cycles. Using a model such as B-SOSE, which assimilates both the physical and the biogeochemical states, instead of a nonassimilating forward model has the advantage of reducing the disparity between observations and model output, in both the ocean circulation and the carbon system. Development of the biological-physical coupled B-SOSE was preceded by the necessary step of a nonoptimized, forward and quasi-steady state simulation. Comparison of this forward model and B-SOSE (Appendix A) provides insight for other unconstrained climate models, whose improvement is one of the goals of SOCCOM.

Here we diagnose the DIC budget in B-SOSE at each model horizontal point integrated over the top 650 m, and contrast the budget in three different regions: the subtropics, the ACC, and the Antarctic. An analysis of the significance of each component of the carbon budget is given on temporal scales ranging from 10 days to 5 years. The analysis here is the first application of the newly developed B-SOSE [Verdy and Mazloff, 2017] to the Southern Ocean DIC budget, and the first intensive analysis of that budget in a state estimate. This analysis provides a hypothesis on the order of magnitude of the different components of the DIC budget, as well as the locations of major spatial and temporal variations in the budget components. These can inform both the interpretation of observations such as from SOCCOM biogeochemical (BGC) floats as well as deployment planning for future BGC floats, in addition to providing an independent validation for climate models with biogeochemistry.

2. Methods

The Biogeochemical Southern Ocean State Estimate (B-SOSE) [Verdy and Mazloff, 2017] is a $1/3^{\circ}$ physical-biogeochemical data-assimilating model that currently covers the years 2008–2012, and which is publicly available at http://sose.ucsd.edu/bsose_solution_Iter105.html. B-SOSE uses the adjoint method to optimize the model, minimizing a weighted least squares sum of the misfits between the model solution and observations. Observations include both physical and biogeochemical properties and come from several sources including Argo floats [Gould et al., 2004], biogeochemical Argo (BGC-Argo) (<http://runt.ocean.washington.edu/o2>), instrumented Southern elephant seals (<http://biology.st-andrews.ac.uk/seaos>), the World Ocean Atlas 2013 (WOA) [Garcia et al., 2014a, 2014b], the GLODAP version 2 (GLODAPv2 hereafter) in situ product [Key et al., 2015; Olsen et al., 2016], the Surface Ocean CO₂ Atlas (SOCAT) version 4 [Bakker, 2016], sea surface height observations from the Radar Altimetry Database System, sea ice concentration from the National Snow and Ice Data Center [Meier et al., 2016], conductivity-temperature-depth sections and expendable bathythermographs.

B-SOSE is developed from the previous $1/6^{\circ}$ SOSE of Mazloff et al. [2010], but with half the resolution, and is part of an ongoing modeling effort toward the development of a $1/12^{\circ}$ resolution state estimate. The lower resolution B-SOSE has been a necessary development step, which also included a biogeochemical forward model that is similar to B-SOSE but without constraints (Appendix A). B-SOSE is spun up for 3 years and then optimized, using the adjoint method. The procedure to assimilate data requires extensive testing, and by reducing resolution the computational cost is considerably diminished. Despite the lack of eddies at this lower resolution, the analysis gives important insights into the large-scale carbon system in the Southern Ocean. Furthermore, even with the reduced resolution, the B-SOSE solution constrained to available observations can be used as validation for other forward biogeochemical models.

The B-SOSE physical configuration is described in section 2.1. Section 2.2 gives an overview of the biological model. Readers are referred to Verdy and Mazloff [2017] for further details of the model configuration of B-SOSE.

2.1. The Physical Model

The physical state of the Southern Ocean in SOSE is simulated using the MITgcm [Marshall et al., 1997], with a domain that spans from 78°S to the equator. The purely physical SOSE has a resolution of $1/6^{\circ}$, 42 vertical levels, and covers the years 2005–2010 [Mazloff et al., 2010]; it has been used in a very large number of studies [e.g., Abernathey et al., 2016; Masich et al., 2015; Tamsitt et al., 2016]. B-SOSE, which is a separate state estimate in the same family, is configured using a Mercator projection with $1/3^{\circ}$ resolution, which provides 32 km resolution at about 30°S and reaches 8 km by 78°S , while from 30°S to the equator the resolution telescopes out. Resolved instabilities do not include the most energetic mesoscale eddies at the first baroclinic Rossby radius: the baroclinic Rossby radius varies from 35 km at approximately 26.6°S to approximately 6 km at 75°S [Chelton et al., 1998]. The model does not include any mesoscale eddy parameterization and thus underrepresents mesoscale structures. Thus B-SOSE can only be used to investigate large-scale processes in the Southern Ocean. The vertical grid is a z-coordinate with 52 vertical levels of thickness ranging from about 4 m at the surface to 400 m in the abyss. The model covers years 2008–2012, with a time step of 1 h. Diagnostics are stored in 5 day averages.

Realistic topography from the 1 arc min global relief model ETOPO1 [Amante and Eakins, 2009] is implemented in the model. Partially filled cells [Adcroft et al., 1997] are used to represent bathymetry, with a quadratic bottom drag with a value of 0.002.

Initial conditions merge SOSE [Mazloff et al., 2010] and the global state estimation of ECCO version 4 [Forget et al., 2015], in order to cover the latitude band from the northern boundary of SOSE (25°S) to the equator. The global atmospheric ECMWF ERA-interim reanalysis of Dee et al. [2011] provides the first-guess atmospheric state at a time step of 6 h. This forces the model using the bulk formulae of Large and Yeager [2009]. Through the adjoint method, the atmospheric state is then adjusted to better fit the observations. River and Antarctic discharges are implemented using the freshwater continental runoff mixed product of Dai and Trenberth [2002] and an estimated distributed Antarctic discharge from Hammond and Jones [2017]. To represent ice dynamics and thermodynamics, an ice component, formulated in Losch et al. [2010] and Fenty

Table 1. Physical Parameters Used in the Physical-Biogeochemical State Estimate of the Southern Ocean (B-SOSE) [Verdy and Mazloff, 2017]

Description	Lateral	Vertical
Tracer advection scheme	Third-order direct space and time scheme	Third-order upwind scheme
Background eddy viscosity	$10 \text{ m}^2 \text{ s}^{-1}$	$10^{-3} \text{ m}^2 \text{ s}^{-1}$
Leith biharmonic viscosity factor	2	
Salinity and temperature harmonic diffusivity	$10 \text{ m}^2 \text{ s}^{-1}$	$10^{-4} \text{ m}^2 \text{ s}^{-1}$
Salinity and temperature biharmonic diffusivity	$10^{10} \text{ m}^4 \text{ s}^{-1}$	
Tracer harmonic diffusivity	$1 \text{ m}^2 \text{ s}^{-1}$	$10^{-5} \text{ m}^2 \text{ s}^{-1}$

and Heimbach [2013], is coupled to the ocean model. Additional physical parameters implemented in the simulation are summarized in Table 1.

2.2. The Biogeochemical Component

The biogeochemical component of B-SOSE is derived from the *Biogeochemistry with Light, Iron, Nutrient, and Gases* model (BLING) [Galbraith et al., 2010]. BLING includes eight tracers: DIC, alkalinity, oxygen, iron, and inorganic and organic forms of nitrogen and phosphorus. Tracers are initialized from the following sources: DIC and alkalinity from the GLODAPv2 climatology [Lauvset et al., 2016; Key et al., 2015]; oxygen, silicate, nitrogen, and phosphorus from the World Ocean Atlas 2013 climatologies [Garcia et al., 2014a, 2014b]; iron, dissolved organic matter, and dissolved organic nitrogen and phosphorus from a coarse resolution coupled model simulation with BLING version 2 (E. Galbraith, personal communication). Additionally, the model includes aeolian iron deposition data from Mahowald et al. [2005]. Atmospheric pCO₂ is from the CarbonTracker product [Peters et al., 2007]. Surface pCO₂ is diagnosed explicitly via carbonate chemistry [Williams and Follows, 2011] and air-sea CO₂ flux is parameterized following Wanninkhof [1992].

Primary production converts DIC into organic matter. Three types of phytoplankton are represented: small (B_{sm}), large (B_{lg}), and diazotrophs (B_{dia}). The biomass in each population, i , is diagnosed in the model according to

$$\frac{\partial B_i}{\partial t} = (\mu_i - \lambda) B_i, \quad (1)$$

where

$$\mu = P_{C_0} L_i (\min[L_{NO_3}, L_{PO_4}, L_{Fe}]) e^{kT} \quad (2)$$

is the growth rate and λ the decay rate

$$\lambda_i = \lambda_0 \left(\frac{B_i}{B_0} \right)^n e^{kT}. \quad (3)$$

P_{C_0} is the maximum photosynthesis rate; L_i , L_{NO_3} , L_{PO_4} , L_{Fe} are functions describing limitation by light, nitrate, phosphate, and iron, respectively; λ_0 and B_0 are constants; k is a constant chosen according to Eppley [1972]; T is temperature. The power-law dependence in the loss function (3), with the exponent set to $n = 3$ for large cells and $n = 1$ for small cells, is based on Dunne et al. [2005]. Note that diazotrophs are not limited by nitrate ($L_{NO_3} = 0$) and have the additional constraint of requiring temperatures above 14°C to grow.

Organic matter is distributed among three pools: a fraction becomes dissolved organic matter (DOM), a fraction goes to the microbial loop that is instantaneously recycled in the mixed layer (R_{ML}), and the remaining fraction sinks as particulate organic matter (POM) and is instantaneously remineralized deeper in the water column (R_{POM}). The fraction of sinking particles depends on phytoplankton size [Dunne et al., 2005; Galbraith et al., 2010]. DOM is remineralized at a constant rate, r . Net community production (NCP) is defined as the difference between the local rates of production and remineralization,

$$NCP = \mu_{sm} B_{sm} + \mu_{lg} B_{lg} + \mu_{dia} B_{dia} - R_{ML} - R_{POM} - rDOM. \quad (4)$$

The change in DIC due to biological activity is

$$\frac{\partial DIC}{\partial t} = NCP + \frac{\partial CaCO_3}{\partial t}, \quad (5)$$

where the change in calcium carbonate ($CaCO_3$) results from shell formation by small phytoplankton. It is expressed as

$$\frac{\partial CaCO_3}{\partial t} = (Ca : C) \mu_{sm} B_{sm} f - D, \quad (6)$$

where $(Ca : C)$ is the stoichiometric ration of calcium to carbon, f is the fraction of small phytoplankton production that becomes POM, and D is the dissolution.

More details on the biogeochemical model formulation can be found in *Galbraith et al.* [2010] and *Verdy and Mazloff* [2017], in particular their Table 1. Simulated biogeochemical fields have been extensively validated in *Verdy and Mazloff* [2017] against in situ observations and climatologies (World Ocean Atlas 2013v2 of *Garcia et al.* [2014a, 2014b] and GLODAPv2 product of *Key et al.* [2015] and *Lauvset et al.* [2016]), and comparisons can also be found at http://sose.ucsd.edu/bsose_valid.html. Results in *Verdy and Mazloff* [2017] show that B-SOSE captures the large-scale patterns of carbon, oxygen, and nutrients.

2.3. Dissolved Inorganic Carbon Budget

The upper ocean DIC budget is computed and closed at each grid point using 5 day averages, and then averaged over 650 m depth. This depth was chosen to include the deepest modeled mixed layer, as in *Tamsitt et al.* [2016]; below this depth the spatially averaged DIC temporal variance is reduced by more than 70% (not shown for brevity).

The time variation of DIC is derived by the three-dimensional tracer conservation equation

$$\frac{\partial DIC}{\partial t} = ADV + DIFF + BIO + F_{CO_2} + DILUT, \quad (7)$$

where ADV is the divergence of advective DIC transport (i.e., $ADV = -\nabla \cdot (\bar{u} DIC) = -\bar{u} \cdot \nabla DIC$, where \bar{u} is the 3D velocity); $DIFF$ are diffusive processes ($DIFF = \nabla \cdot (\kappa \nabla DIC)$, where κ is the parameterized diffusivity, sum of horizontal and vertical components with background values listed in Table 1); BIO are the biological mechanisms including sources and sinks due to uptake, respiration, and calcium carbonate shell dissolution (equation 5)); F_{CO_2} is the air-sea CO_2 exchange; and $DILUT$ is the change of concentration caused by change of the volume of freshwater from precipitation, river input, sea ice formation and melt, and evaporation.

Velocity and DIC can be separated into the mean (computed over 5 years and indicated by an overbar) and fluctuations (i.e., deviations from the mean, indicated by $'$), following the Reynolds decomposition:

$$\bar{u} = \bar{u} + u'$$

and

$$DIC = \overline{DIC} + DIC'.$$

Fluctuations represent the anomaly from the mean state, and contain a mix of seasonal cycle, interannual variability, and model drift. Decomposing then the velocity into its horizontal (with suffix h) and vertical (w) components, the advective term becomes,

$$\overline{ADV} = -\overline{\bar{u} \cdot \nabla DIC} = -\overline{\bar{u}_h} \cdot \nabla_h \overline{DIC} - \overline{w} \frac{\partial \overline{DIC}}{\partial z} - \overline{\bar{u}'_h \cdot \nabla_h DIC'} - \overline{w' \frac{\partial DIC'}{\partial z}}. \quad (8)$$

Furthermore, we divide the horizontal velocity into geostrophic and ageostrophic components, with the latter defined as the residual between the model velocity and the geostrophic term: $\bar{u} = \bar{u}_g + \bar{u}_a$, where $\bar{u}_g = (-\frac{1}{f\rho_0} \frac{\partial p}{\partial y}, \frac{1}{f\rho_0} \frac{\partial p}{\partial x})$, with f the Coriolis parameter, ρ_0 a reference density, and p the model pressure. The ageostrophic term is primarily associated with wind-driven Ekman transport, which sets its large-scale features, and with local effects due to the interaction between the flow and the topography. These terms will be diagnosed in section 3.3.

3. Results

The goal of this work is to identify the large-scale processes impacting the spatial and temporal structure of DIC concentration in B-SOSE. One caveat is that, due to the model resolution and the absence of sophisticated parameterizations, mesoscale eddies and submesoscale processes are poorly represented. Unless otherwise specified, temporal means are computed over 5 years from January 2008 to December 2012, and vertical averages calculated over the upper 650 m (indicated by the $\langle \cdot \rangle$ symbol).

The latitudinal extent of the analysis region is 26.6°S–78°S. We divide this into three domains, characterizing the main features of each region and highlighting the differences between them. The regions (Figure 1) are (1) the ACC (blue shaded in figure), (2) the subtropical region north of the ACC (red), and (3) the Antarctic region south of the ACC (in gray, with the Weddell Gyre highlighted in green). The ACC boundary limits are chosen using the northern and southernmost uninterrupted mean model sea surface height contours through the Drake Passage (Figure 1). We use these as proxies for the Subantarctic (north) and the Southern ACC fronts (south), following Tamsitt *et al.* [2016, section 2.b].

A series of figures showing the misfit between B-SOSE and observations is available at http://sose.ucsd.edu/bsose_valid.html. Here the reader can find profiles, horizontal maps, and vertical sections of the difference in time and space between model output and observations. Overall, there is good agreement between B-SOSE and observations; however, there are some locations where the misfit is large, hypothesized to be due to model errors in the physical circulation. Though the misfit magnitudes are steady in time, B-SOSE DIC does exhibit a drift. Northeast of the Drake Passage and at midlatitudes in the Indian Ocean, misfits are significant and the drift is likely spurious. Elsewhere, the drift may be part of a natural change in the carbon system. For the present analysis, we do not remove the linear drift in order to preserve a representation of the natural drift of the carbon system.

3.1. Mean and Variance of DIC

The time and depth (0–650 m) average DIC concentration ($\langle \text{DIC} \rangle$, Figure 2a) has a meridional gradient structure, with largest concentrations in the Weddell and Ross Seas, where carbon-rich deep waters from the northern basins have upwelled and fill the upper water column, and lowest values in the subtropics, where carbon and nutrients have been heavily utilized in the upper water column. The DIC inventory compares well with the GLODAPv2 product of Key *et al.* [2015] and Lauvset *et al.* [2016] (Figure 2b), though the

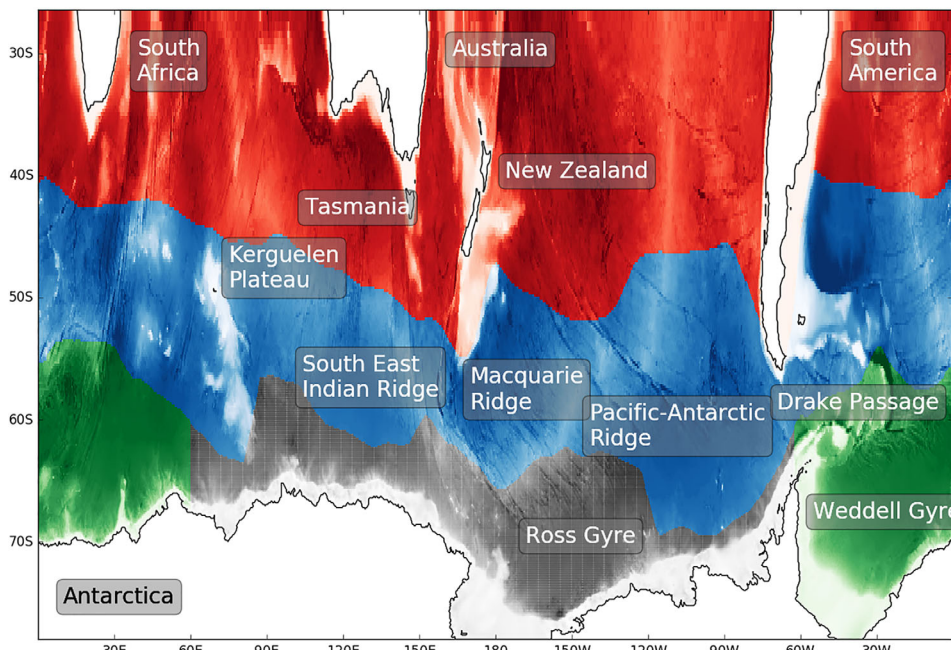


Figure 1. Southern Ocean bathymetry (ETOPO1) [Amante and Eakins, 2009], color coded based on the region: subtropical region (red), ACC core (blue), Weddell Gyre (green), and the remaining area south of the ACC (Antarctic region, in gray). Black contours are coastlines.

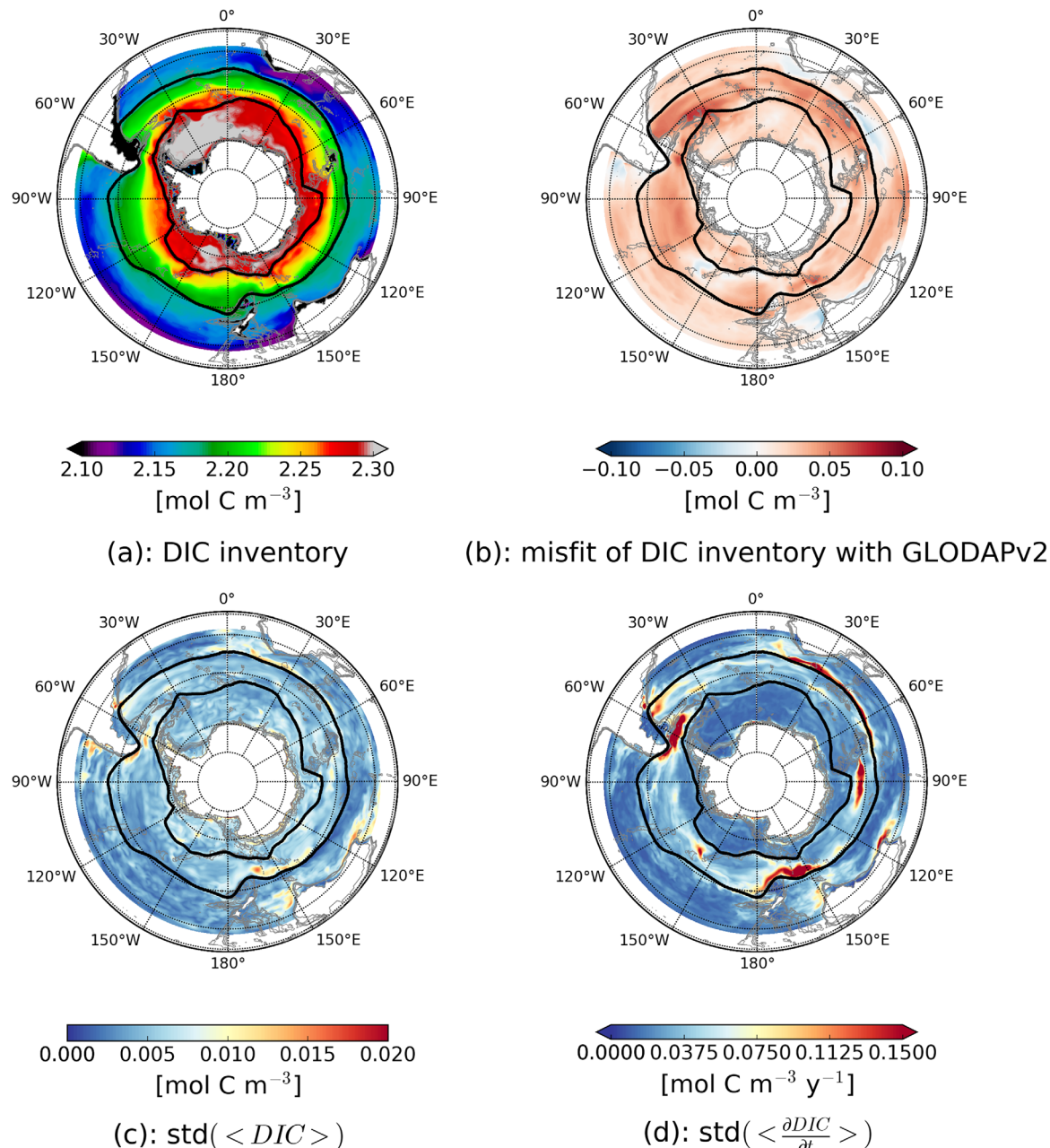


Figure 2. (a) 5 year and 0–650 m averaged concentration of DIC ($\langle \bar{DIC} \rangle$). (b) Difference ($\langle \bar{DIC} \rangle - \langle \bar{GLODAPv2} \rangle$) from GLODAPv2 [Key et al., 2015; Lauvset et al., 2016]. (c) Standard deviation of $\langle \bar{DIC} \rangle$ and of the (depth averaged) tendency of DIC (d), computed over a period of 5 years. Gray contours are 0, 600, 1200, 1800, 2400, and 3000 m isobaths. Black contours are the ACC boundaries, as defined in section 3.5.1.

DIC in B-SOSE is biased high by several percent over most of the domain, likely due to the fact that the model represents 2008–2012, whereas GLODAPv2 bins observations (primarily collected in summer) that span a temporal range from 1973. The largest differences from GLODAPv2 are east of the Drake Passage and south of Tasmania, where the model exceeds the GLODAPv2 product by about 0.7 mol C m^{-3} (note that the color in figure is saturated), over the Pacific-Antarctic Ridge (approximately at 150°W), and in the Indian Ocean at $\sim 60^{\circ}\text{E}$, where the model has a deficit of $\sim 0.2 \text{ mol C m}^{-3}$ with respect to the product.

Figures 2c and 2d show the temporal DIC variability in B-SOSE, computed as the standard deviation of $\langle \bar{DIC} \rangle$ (panel c), and of its rate of change ($\langle \frac{\partial \bar{DIC}}{\partial t} \rangle$, panel d), over the 5 year model span. The variability is concentrated in several hot spots: the Brazil-Malvinas confluence (60°W – 45°W), east of the Drake

Passage, east of Kerguelen Plateau ($\sim 75^{\circ}\text{E}$ – 105°E) and along the Subantarctic Front in the Indian Ocean, the subtropical Pacific between 135°E and 150°E , between the Southeast Indian Ridge and Macquarie Ridge (150°E – 170°E), and near the Pacific-Antarctic Ridge (around 150°W). The causes for such hot spots are the focus of the next sections.

3.2. Mean Carbon Budget Terms

Focusing on the time and depth average terms determines which terms sustain the mean state and its variance (Figure 3). Overall, *ADV* is the largest term (Figure 3a) and balances the mean DIC tendency (*TEND* hereafter) in several locations (Figure 3f). We find a small positive change in the mean tendency of DIC, the aforementioned drift, which is simply the variation between the final and the initial timesteps. The maximum increase found at the end of the simulation ($\sim 0.013 \text{ mol C m}^{-3} \text{ yr}^{-1}$) is in the ACC south of New Zealand, which corresponds to a change of about 0.5% from the initial state. Atmospheric CO₂ increases in time, and we expect some oceanic trend in response.

We discuss the general budget in three regions:

In the Antarctic Circumpolar Current the tendency of DIC (Figure 3f) and the *ADV* term (Figure 3a) show a similar spatial pattern, indicating *ADV* is the main driver of the *TEND* variability. Significant *ADV* DIC supply occurs in the Southern ACC Front region in the Indian Ocean, and also at the Malvinas and southwest of South America. *DIFF* increases DIC in the northern part of the ACC and decreases it in the southern part (Figure 3b). Small-scale structures with large values of *DIFF* are associated with meandering fronts. *BIO*

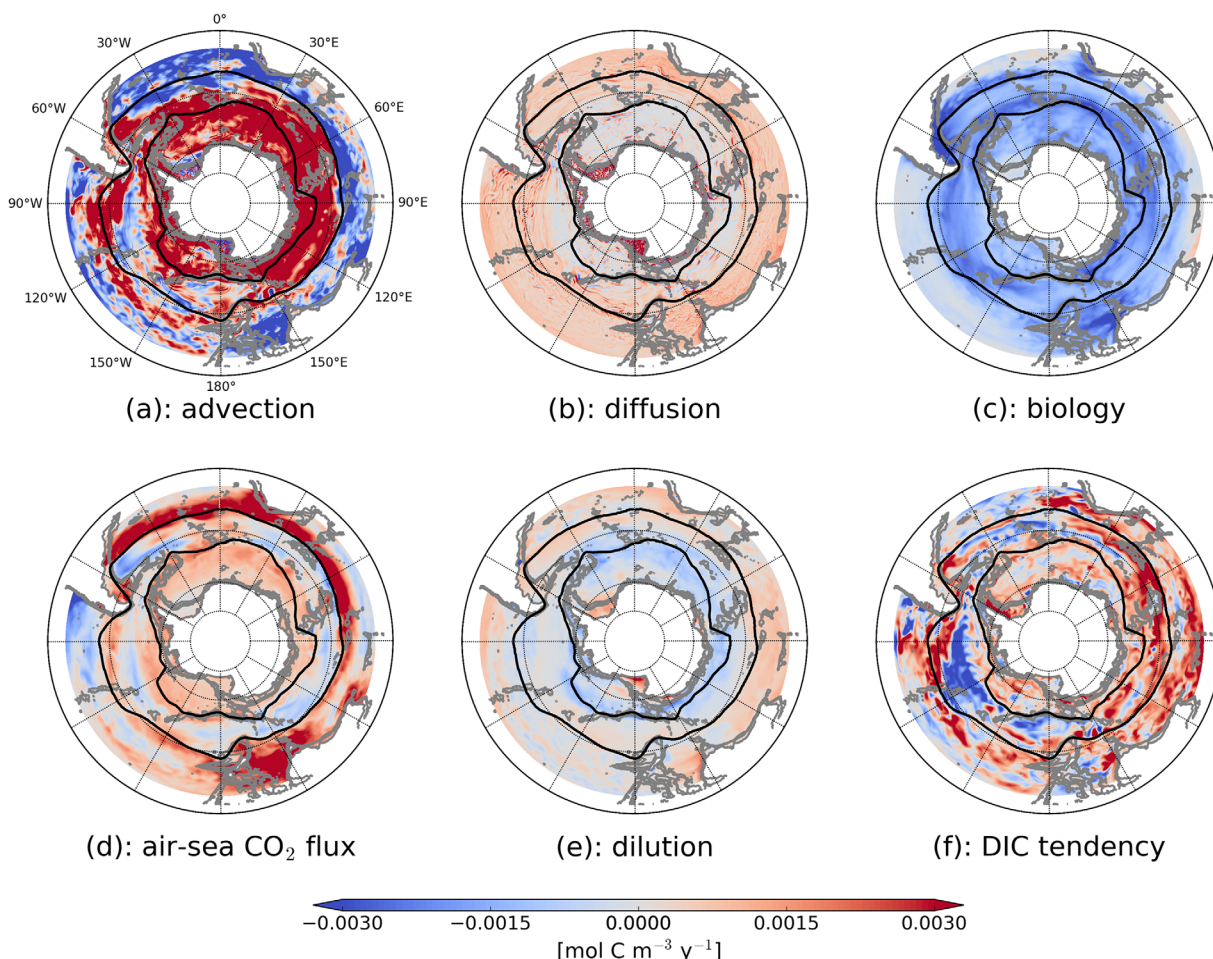


Figure 3. Temporal averages of the terms of equation (7): (a) advective and (b) diffusive transports, (c) biological mechanisms (negative values represent carbon depletion due to biological productivity), (d) air-sea exchange (positive values indicate ocean uptake), (e) surface freshwater flux, and (f) tendency of DIC. Figures 3a–3c and 3f are also 0–650 m averages. Gray contours are 0, 600, 1200, 1800, 2400, and 3000 m isobaths. Black contours indicate the ACC boundaries. Saturated values permit better visualization.

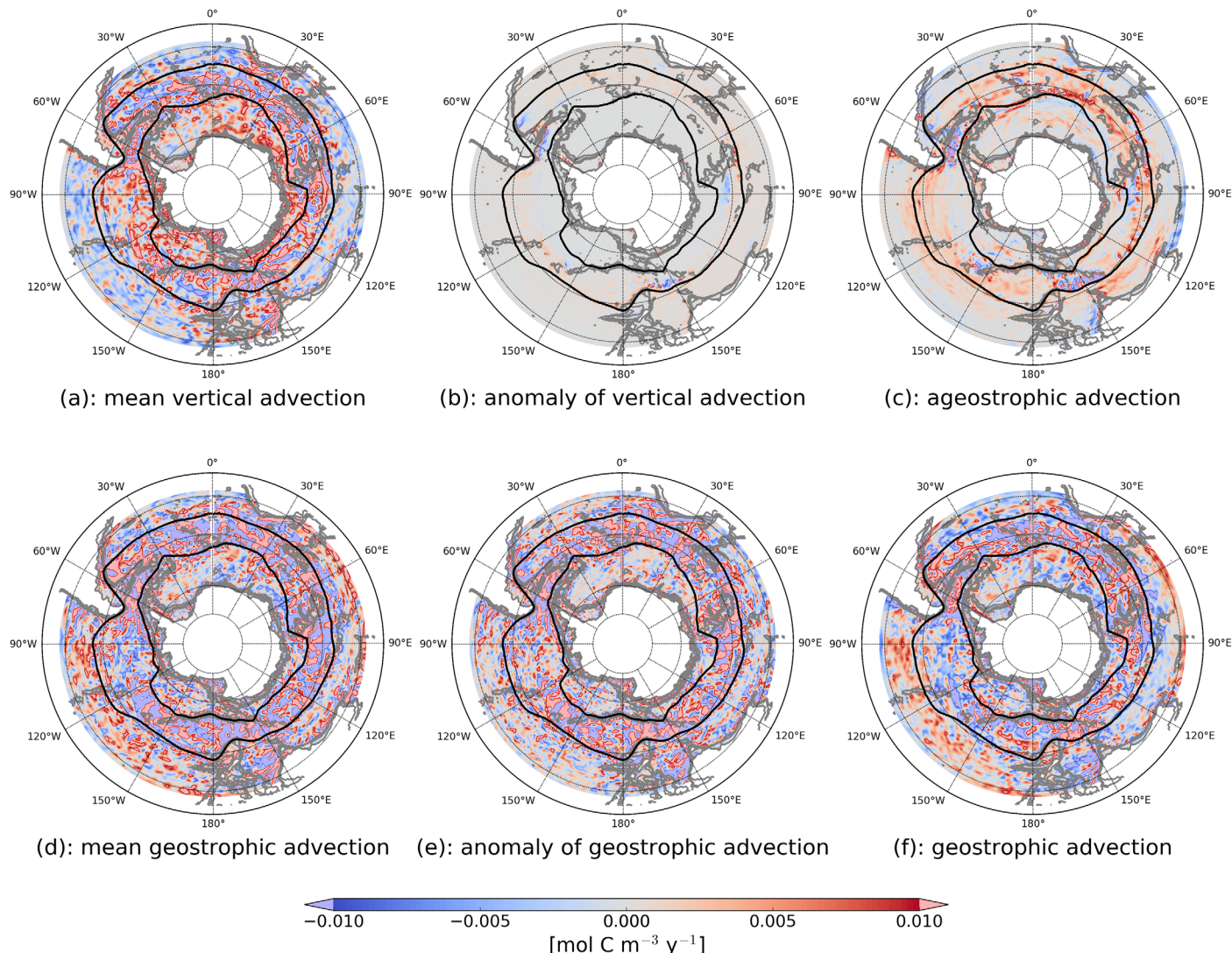


Figure 4. Divergence of advective DIC transport, given as time (5 years) and depth average (0–650 m), and divided into (a–b) vertical and (c–f) horizontal components. The horizontal term has been divided into (c) ageostrophic and (d–f) geostrophic terms. The geostrophic components are shown as (d) mean, (e) anomaly from the mean and (f) sum of the two. Gray contours are 0, 600, 1200, 1800, 2400, and 3000 m isobaths. Black contours indicate the ACC boundaries. Saturated values are shown with transparency, in order to allow the visualization of the structures beneath. (a) $\bar{w} \frac{\partial \text{DIC}}{\partial z}$ is the mean vertical advective transport of DIC, (b) $\bar{w}' \frac{\partial \text{DIC}}{\partial z}$ is the anomaly of the vertical advective transport of DIC, (c) $\bar{u}_a \cdot \nabla_h \text{DIC}$ is the mean ageostrophic transport of DIC, (d) $\bar{u}_g \cdot \nabla_h \text{DIC}$ is the mean geostrophic advection of DIC, (e) $\bar{u}'_g \cdot \nabla_h \text{DIC}$ is the anomaly of the geostrophic advection of DIC, and (f) $\bar{u}_g \cdot \nabla_h \text{DIC}$ is the total geostrophic advection of DIC.

(Figure 3c) is negative everywhere in the ACC, reflecting that draw down by biological production is larger than remineralization. Air-sea CO₂ flux increases DIC along the southern part of the ACC, in the Malvinas Current, in the central Atlantic sector, and along the Subantarctic Front in the Pacific sector. DILUT reduces the concentration of DIC near the southern ACC boundary, due to both precipitation and sea ice melt (see Figure 5d and the blue spots crossing the southern ACC Front in Figure 3e). DILUT drives an increase in DIC concentration in the northern part of the ACC due to net evaporation.

In the subtropical region the ADV term (Figure 3a) reduces DIC except in the Brazil Current and in the South Pacific. ADV is again the largest term and is in part balanced by DIFF, F_{CO₂}, and DILUT (Figures 3b, 3d, and 3e). In boundary currents, southeast of Australia and north of the Subantarctic Front not only ADV, but also other mechanisms, described below, have a large impact on the DIC. Overall, diffusive processes supply DIC to the upper ocean (Figure 3b), whereas B/O drives a sink of DIC in the very productive boundary currents in the South Atlantic and southern Indian Oceans. Elsewhere, B/O is largely reduced and, in the northernmost areas of the Indian and Atlantic Oceans, remineralization drives a supply of DIC. The F_{CO₂} term

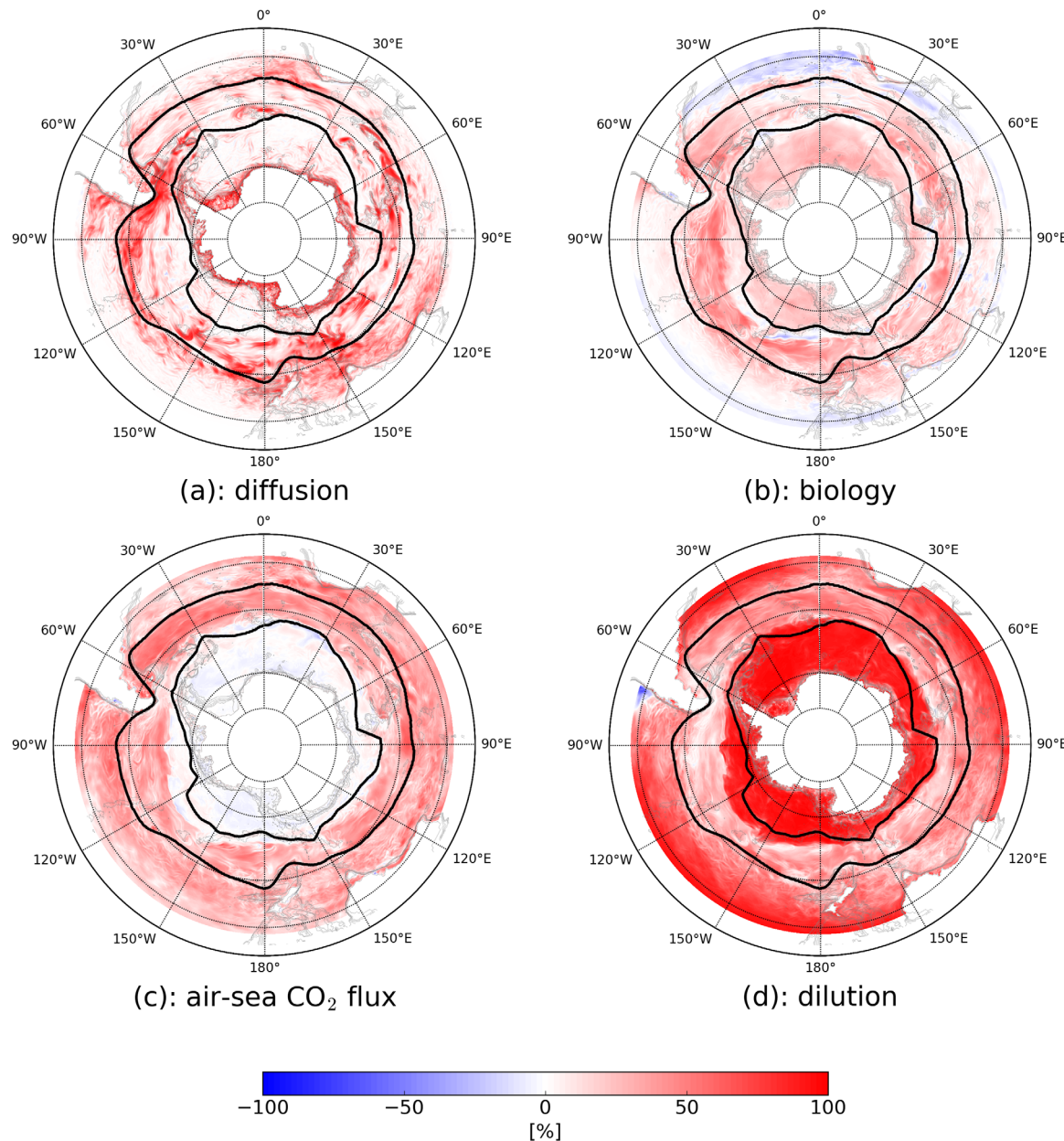


Figure 5. Variance of the material derivative, $TEND + ADV$, explained by (a) diffusion, (b) biological processes, (c) air-sea CO_2 flux, and (d) freshwater flux. Gray contours are 0, 600, 1200, 1800, 2400, and 3000 m isobaths. Black contours indicate the ACC boundaries.

(Figure 3d) shows patterns of opposite sign in each basin, however the carbon uptake in boundary currents and in the productive area south-east of Australia is larger than the net outgassing in this region, and the net effect results in a net uptake (shown in the following section 3.5.2). Finally, the $DILUT$ component (Figure 3e) increases the overall upper ocean DIC concentration due to evaporation, but areas in which the concentration decreases due to precipitation are also present, and appear mostly in the Pacific sector.

In the Antarctic region ADV likewise dominates the local balance, setting the mean $TEND$. In general, ADV is a source of carbon, as is F_{CO_2} , while biological production and dilution (precipitation and sea ice melting) act as sinks of carbon concentration. An exception to this generality is at the Antarctic continental shelf. Here air-sea CO_2 fluxes (Figure 3d) can be as important as ADV . Furthermore, $DILUT$ (Figure 3e) is large and positive almost everywhere due to sea ice formation and export. For a given volume of water, sea ice formation increases the concentration of DIC. The model does not represent DIC uptake and advection by sea ice,

nor any other drivers of DIC dynamics in the sea ice, such as entrapment of DIC during sea ice formation, precipitation/dissolution of ikaite, or bubbles of CO₂ formed in brine, which directly affect DIC [Moreau *et al.*, 2015]. Nevertheless, the effects of such assumptions in the model are small, as approximately 80% of DIC is naturally rejected by brine convection to the ocean [Moreau *et al.*, 2015]. DIFF (Figure 3b) is also important near the continent, largely due to the horizontal component (not shown for brevity). Similarly, the B/O sink of DIC is influential in this region (Figure 3c).

In summary, almost everywhere ADV is the most important component setting the local mean state of TEND. However, there are numerous regions where the other components have equal importance.

3.3. Influence of Ocean Circulation on DIC

The impact of ocean circulation on the tendency of DIC (i.e., the ADV term in equation 8) is here analyzed in its components. Figure 4 shows the temporal and vertical average of ADV, $-\langle \bar{u} \cdot \nabla DIC \rangle$, divided into vertical (panels a and b) and horizontal (c–f) components. A Reynolds decomposition of velocities and DIC is used to separate time means and anomalies, as described in section 2.3. The horizontal velocity has also been partitioned into ageostrophic (c) and geostrophic (d–f) components. Black contours in the figure are the ACC boundaries, defined above.

Each component of ADV has a large magnitude and is important for the tendency of DIC, except $\langle w' \frac{\partial DIC}{\partial z} \rangle$ (Figure 4b). The vertical component, in which the mean (Figure 4a) represents the main constituent, reflects the large-scale wind-driven upwelling south of the Subantarctic Front, which brings deep and carbon-rich waters to the surface, and subduction of surface waters below 650 m in the subtropical region. However, smaller structures superimposed on this large-scale pattern have a strong impact in locations of large kinetic energy, such as over or next to prominent topographic features [Chelton *et al.*, 1990].

The ageostrophic component (Figure 4c), which in the open ocean is associated with the wind-driven Ekman velocity, decreases rapidly from the surface to approximately 80 m, below which it is large only in locations of strong interaction with the topography (not shown). The positive values of $-\langle \bar{u}_a \cdot \nabla_h DIC \rangle$ in the ACC are explained by northward ageostrophic velocity acting on a negative gradient of DIC, as DIC decreases northward (Figure 2a). This represents an ageostrophic wind-driven transport of carbon-rich waters from Antarctica toward the subtropics (Figure 2a). Meanwhile in boundary currents, such as the Agulhas and the East Australian currents, the ageostrophic advection acts to export DIC from the subtropics via viscous and nonlinear dynamics.

The mean (Figure 4d) and anomaly (Figure 4e) of the geostrophic advection (Figure 4f), which is the sum of panels d and e, are largest in the ACC and in the presence of boundary currents (Agulhas, Malvinas, and East Australian currents). The presence of topography induces the largest hot spots, particularly in the ACC (Figure 4f). Near the Drake Passage and the Pacific-Antarctic Ridge the mean geostrophic component is compensated by the mean vertical advective term (Figure 4a).

The components of ADV have large magnitudes in several hot spots, but largely balance each other in these regions such that only the large-scale pattern emerges in the total mean of ADV (Figure 3a). In particular, ADV is largely due to the vertical processes of upwelling south of the Subantarctic Front and downwelling north of it. Ageostrophic flow exports DIC from the Antarctic waters, which contributes to the positive values of the mean ADV in the ACC (Figure 3a) and, together with the geostrophic transport, north of the Subantarctic Front in the Pacific sector. Finally, mean vertical advection and geostrophic flow supply DIC in the Malvinas Current, while the geostrophic component drives the largest export of DIC in the East Australian Current and in the Benguela current.

3.4. Drivers of the DIC Temporal Variability

We have given a qualitative view of how the different processes force the mean rate of change of DIC, or TEND. The correlation between the different components is complex and warrants a more detailed analysis. In this section, we focus on the drivers of the temporal variability of the TEND term, shown in Figure 2d.

3.4.1. Variance Explained

In order to understand what processes drive the temporal variability of the DIC concentration and its change with time $\frac{\partial DIC}{\partial t}$, we compute the variance explained, a metric that assesses the consistency of both the phase and magnitude of two time series, g and f , as

$$VE = 100\% \left(1 - \frac{var(g-f)}{var(g)} \right), \quad (9)$$

where $var(\cdot)$ indicates the variance of the term in parenthesis. We find that ADV , represented by f in equation 9, explains approximately 93% of the $TEND$, g , variance everywhere (not shown). Thus, we calculate the material derivative to look at the residual signal: this allows investigating which other processes are important (Figure 5). Near-zero or negative values of variance explained (Figure 5) mean that either f is out of phase with $g=TEND+ADV$ or that the magnitudes are inconsistent, implying that f does not determine how g changes. The largest energy peaks at the annual period and its harmonics scale (supporting information Figure S1), and thus we expect that much of the variance explained represents this signal (further investigated in the next section).

The variance explained by the diffusive transport is localized and only important on small spatial scales (Figure 5a), in particular over shallow or steep topography (gray contours in figure), and in some of the hot spots of the standard deviation of the $TEND$ term (Figure 2d): in the Drake Passage, east of the Kerguelen Plateau and partly in the region east of 150°E. Mainly, this term reflects the horizontal diffusive transport, as the variance in the horizontal component is larger than the variance in the vertical diffusive transport (not shown).

The biological term (Figure 5b) in general explains 50% or less of the variance of the material derivative, except in localized regions. In the subtropics, for example in the Brazil and the Benguela Currents, the VE is approximately 80%. Furthermore, the biological term explains ~50% of the variance in the ACC north of the southern ACC Front, and some variance (less than 30%) in the Antarctic region. In the north part of the subtropical Atlantic Ocean, and close to Tasmania, New Zealand and the Pacific-Antarctic Ridge, the VE by BIO is negative.

Air-sea CO₂ flux (Figure 5c) explains a significant percentage of the variance of the material derivative (with a median value of ~76%). In the Indian sector, the flux shows larger values of VE east of Kerguelen Plateau, meaning that, together with the diffusive transport and biological processes, this term is partly responsible for the large variability of $TEND$ in this region. Air-sea CO₂ flux does not explain the variance of the material derivative in the seasonal sea-ice zone, which extends from Antarctica to just north of the southern ACC Front (see Figures 3e and 5d).

The $DILUT$ term (Figure 5d) explains much of variance of the material derivative everywhere, with the exception of a few locations in the ACC sector, in the Malvinas Current and in the Indian sector close to Australia. The large signal that covers the Antarctic region and crosses through the southern ACC Front into the ACC is the signature of sea ice melt and formation processes, while in the subtropical region it indicates evaporation.

3.4.2. Temporal Scales of Variability

The analysis of the variance explained described above includes all timescales resolved in the 5 year span from 2008 to 2012. Here we separate the variability occurring at different timescales by applying a set of low and high pass Butterworth filters to the budget terms, and then recomputing the VE (equation 9) using the filtered components of g and f . In particular, we are interested in what governs the changes on timescales shorter than 45 days, between 45 and 365 days, and on interannual scales, longer than 1 year (maps in Figure 6). At the annual scale, each mechanism has the largest energy (supporting information Figure S1). However, we expect a large influence from the interannual scale as well [e.g., Landschützer et al., 2014, 2015; Fay and McKinley, 2013]. Again, we find that ADV explains the majority of the $\frac{\partial DIC}{\partial t}$ variability at all timescales, except along the coast of Antarctica for timescales shorter than 45 days (not shown). Therefore, as above, we calculate the variance explained (equation 9) of the filtered material derivative.

At scales shorter than 45 days, the diffusive transport (Figure 6a) explains more than 60% of the variance of the material derivative in a few localized spots and explains no variance elsewhere. The areas with large VE are located southwest of South Africa, south of Australia, in the coastal region of Antarctica and in the three hot spots of large variability of the $TEND$ term (Figure 2d). By looking at longer timescales, the changes in the diffusive transport explain the variance of the material derivative in increasingly larger areas, from 45 to 365 days (central panel of Figure 6a), the $DIFF$ term has significant VE in the central and eastern parts of the subtropical Indian and Atlantic Oceans and in the western part of the subtropical Pacific, in several spots in the ACC, mostly close to topographic features, and in a few locations of the Antarctic region. At interannual

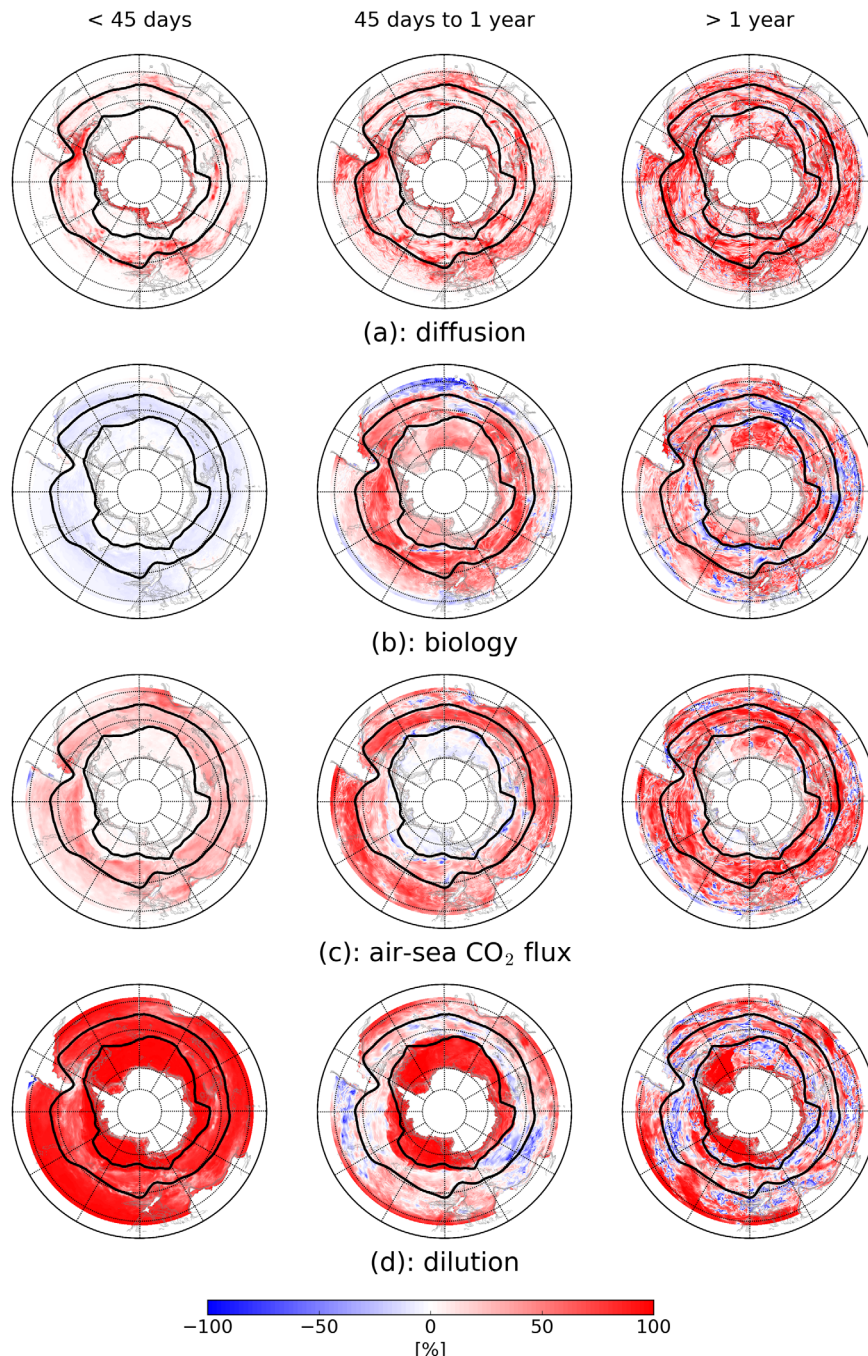


Figure 6. Same as Figure 5, but after applying (left column) a high-pass filter of 45 days, (center) a bandpass filter between 45 days and 1 year, and (right) a low-pass filter of 1 year.

scales (right panel), *DIFF* explains a large amount of the variance of the material derivative over most of the Southern Ocean, with larger values close to coast, topographic features, and boundary currents.

At timescales shorter than 45 days, the biological term (Figure 6b) does not explain the temporal variation of the material derivative of DIC. Between 45 and 365 days, instead, *BIO* uniformly explains some variance of the material derivative in the ACC, except east of the Mid Atlantic Ridge, at 0°. The spatial structure of the VE at these periods reflects the pattern of unfiltered term shown in Figure 5b. By removing the annual cycle, the interannual VE by biological processes shows some patchiness, in particular in the subtropics. We find that *BIO* explains approximately 60% of the variance of the material derivative for timescales longer than 1

year in the south Indian Ocean, in some locations of the Ross and the Weddell Gyres, and southwest of South Africa.

The *VE* by F_{CO_2} for timescales shorter than 45 days (Figure 6c, left) is smaller than 50% in most regions. However, we find *VE* greater than 50% in the Malvinas Current and in the areas southwest of South Africa and between Australia and Tasmania. From 45 days to annual scales (center) the *VE* is mostly larger, especially in the subtropical region and in the ACC. However, the variability of F_{CO_2} still does not explain the variability of the material derivative in the southern part of the Southern Ocean. For timescales greater than 1 year (right) the *VE* by F_{CO_2} shows some large hot spots with values of $\sim 80\%$ in subtropical waters, in the ACC, and in the Antarctic region close to the Polar Front and in the western part of the Weddell Gyre, but low or negligible *VE* in the Ross Gyre and in the eastern side of the Weddell Gyre (Figure 6c).

DILUT (Figure 6d) explains $\sim 100\%$ of the variability of the material derivative for periods shorter than 45 days, except in the Malvinas Current and in the areas west of Tasmania, east of the Kerguelen Plateau and east of the Drake Passage. At scales between 45 and 365 days, the *VE* by *DILUT* is large in the Antarctic region and to north of the southern ACC front. The northern part of the subtropics also shows significant *VE*, while in other regions the *VE* is small or negligible. The interannual variability of *DILUT* explains almost 100% of the variance of the material derivative in the western side of the Ross and Weddell gyres out to the edge of melting sea ice (see Figure 3 and discussion in section 3.1). Large *VE* is also found in the subtropical region, with the exception of a few spots, and in several localized patches of the ACC.

We find that *ADV* explains almost 100% of the temporal variability of *TEND* everywhere in the Southern Ocean, at any timescale (up to 5 years in our study). When one considers the full material derivative, however, the impact of the other components of the carbon budget is revealed. This analysis demonstrates that all the components are important, though their influence varies based on the timescale and location considered. Furthermore, this highlights that observations able to resolve a wide range of temporal scales (from short timescales of the order of few days, to several years) are crucial to capture the temporal variability of the carbon system [McKinley et al., 2017].

3.5. Carbon Budget

In order to quantify the impact that each process has on the tendency of DIC, we analyze the carbon budget. We first look at the volume average of the budget over the whole Southern Ocean and analyze the seasonal cycle (section 3.5.1), which is the most energetic mode of the carbon system variability (supporting information Figure S1). We then focus on the processes in three regions: the ACC, the subtropics, and the Antarctic regions (section 3.5.2) in order to highlight the spatial variability of different mechanisms.

3.5.1. Seasonality of the Southern Ocean Carbon Budget

The seasonal cycle of the volume averaged (from 0 to 650 m and from Antarctica to 26.6°S) DIC budget terms is shown in Figure 7. The decrease in DIC concentration (black curve) in the Austral spring and summer is dominated by the biological sink (red) and dilution due to freshwater input (cyan; either river input and precipitation in subtropical areas, sea ice melt and precipitation close to the southern ACC front, and sea ice melt in the Antarctic region). Overall, we find a net ocean uptake of DIC driven by air-sea CO_2 flux (magenta; positive values indicate CO_2 flux into the ocean). Diffusive processes, as expected from the previous analysis (sections 3.1 and 3.4), do not have a strong impact on the budget, however they do represent a constant source of DIC to surface waters across 650 m. In the volume average *ADV* is almost negligible in summer, but in colder months (May–November) it is a source of DIC.

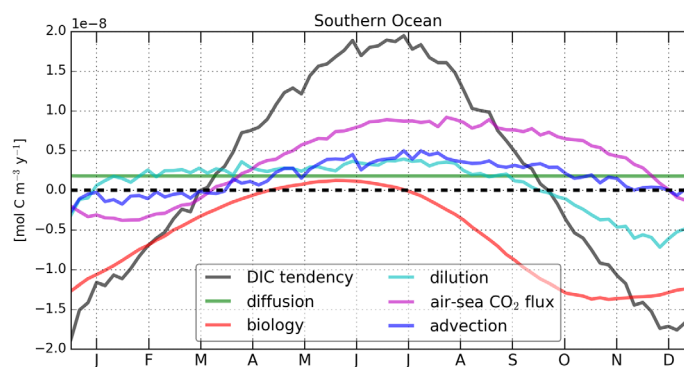


Figure 7. Five year mean seasonal cycle of the DIC budget terms, computed over the entire modeled Southern Ocean (26.6°S–78°S). The DIC tendency (black) is the sum of all terms: divergence of advective transport (blue), diffusive transport (green), biological processes (red), air-sea flux (magenta), and freshwater flux (cyan).

3.5.2. Regional Carbon Budget

To summarize the spatial variability of the mean components of the carbon budget (Figures 2–4), we analyze the budget in three different regions, identified in Figure 1 as the ACC core (section 3.5.2), the subtropical waters north of the ACC (section 3.5.2), and the seasonal ice zone south of the ACC (section 3.5.2). Our aim is to focus on the main spatial features and on the differences between these regions. Unless otherwise indicated, the analysis in the following sections is based on the top 650 m, time average, and latitudinal integration of the budget terms. We show both the 5 year mean and the seasonal cycle of the budget terms. Overall, we find all terms vary significantly in space and time.

3.5.2.1. The Antarctic Circumpolar Current

The DIC budget is here analyzed as a function of longitude. At timescales shorter than 1 year the temporal change of DIC is driven by advection. This term tends to be positive (i.e., increasing the upper ocean DIC concentration) at every longitude in the ACC, except close to rough topography, such as around the south-east Indian Ridge (around 120°E), Macquarie Ridge (east of 150°E), the Pacific-Antarctic Ridge (east of 150°W), and east of the Drake Passage in the Malvinas Current (~50°W). Approximately 1 order of magnitude separates the rate of change of DIC due to the circulation and the other processes. However, this disparity is reduced on longer timescales, as the advective term becomes diminished by time averaging. In what follows we present the 5 year average plot (Figure 8). In the 5 year average the advective term (blue line) is predominantly positive, largely due to the mean ageostrophic and vertical advective components (Figure 4).

Dilution (cyan line) from precipitation reduces DIC, except east of the Drake Passage, where we observe an increase of DIC due to evaporation. Furthermore, sea ice export into the ACC region and melting at specific longitudes (around 60°E, 180, 50°W and 15°W) enhance the *DILUT* further reducing DIC (see darker blue rings representing sea ice melt in Figure 3e and note how they sometimes cross into the ACC). On average, the diffusive transport of DIC (green curve) has a negligible impact in the budget.

Biological processes decrease the DIC concentration over the whole ACC (red). Locations with the largest biological DIC drawdown are the Kerguelen Plateau in the Indian Ocean sector at ~75°E, the eastern Pacific sector (east of 90°W) and the Malvinas Current. The biological drawdown in these locations is expected, as these areas are well-known for the existence of large phytoplankton blooms [e.g., Blain *et al.*, 2007; Moore and Abbott, 2000, 2002], particularly in spring and summer (Figure 9). Peaks of air-sea CO₂ flux occur at the same locations of major biological effect: biological production can in fact drive a net uptake, as in the Kerguelen region [e.g., Jouandet *et al.*, 2008], in the eastern Pacific and close to the Drake Passage. In addition, east of the Drake Passage there is net outgassing at the location of the Malvinas bloom area. Outgassing and biological production are here associated with evaporation and nutrient supply by ocean circulation.

Analyzing the seasonal cycle sheds light on the temporal variability of the budget (Figure 9). The *ADV* term has much larger amplitude than the other terms, and as such we present the material derivative, which is the sum of the *ADV* term with the DIC tendency. For each season, we also calculate the volume integrals of

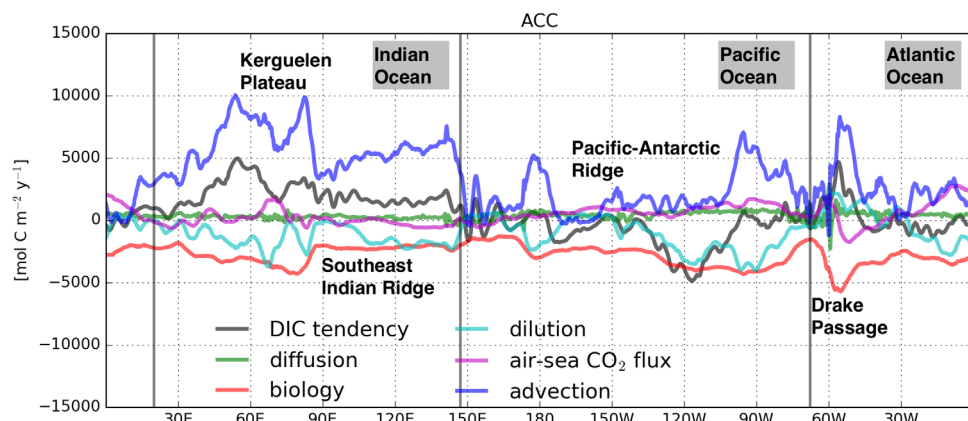


Figure 8. Temporal mean (5 years) of the DIC budget terms in the ACC region, vertically averaged over depth (0–650 m) and integrated over the ACC latitudinal extent. The DIC tendency (black) is the sum of all terms: divergence of advective transport (blue), diffusive transport (green), biological processes (red), air-sea flux (magenta), and freshwater flux (cyan).

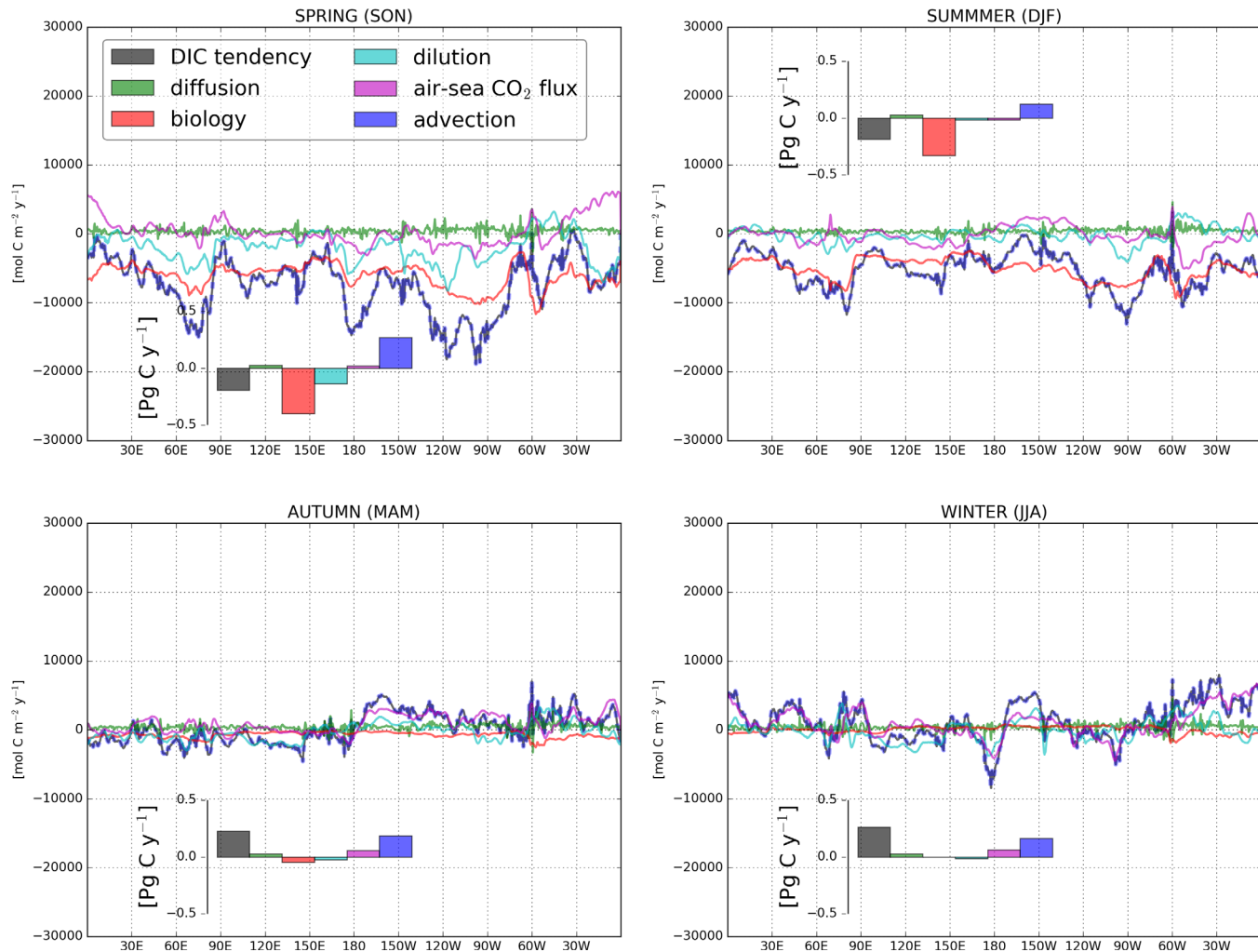


Figure 9. The DIC budget terms for the ACC region, divided into Austral seasons, and color coded as in Figure 7. Note that for clarity, the advective term has been summed to the tendency term (i.e., the black and blue line shows the material derivative). The inset plots in each panel show the net spatial and time integral of each term of the budget (here the advective transport is shown separately from the tendency term).

the different processes (histograms in Figure 9): here *TEND* (in black) and *ADV* (blue) terms are presented separately.

In spring, biological production and export of particulate organic carbon along with *DILUT* from precipitation and sea ice melt drive the material derivative (Figure 9). When integrated over the domain (see the histogram), the net carbon drawdown due to biological uptake and dilution by precipitation and sea ice melt is largely balanced by the supply from the *ADV* term. On average, we find that the net effect of the F_{CO_2} drives a small uptake of DIC, which is mostly due to the large DIC uptake in the Atlantic sector and east of the Kerguelen Plateau.

In summer, biological production strongly influences the spatial variability of the material derivative. Both *DILUT* and air-sea CO_2 flux show a large variability in longitude. In some locations, such as at the Kerguelen Plateau or east of the Drake Passage, these two terms balance each other. Overall, the net effect of the *DILUT* and the carbon flux is small, as regions of evaporation are balanced by precipitation, and outgassing is balanced by ingassing. Also, the *ADV* term contributes to the supply of DIC, but overall the ACC budget in summer shows a net loss of DIC, mostly due the strong drawdown of carbon by biological production.

In autumn, biological export of particulate organic carbon continues, but its magnitude is decreased with respect to the warmer months. The largest impact still occurs at the Kerguelen Plateau and east of the Drake Passage. Overall, *DILUT* and air-sea CO₂ flux, which both show a large longitudinal variability, drive the material derivative of DIC. The *DILUT* term mostly represents precipitation, except in the Pacific sector and east of the Drake Passage, which are areas of net evaporation. Carbon air-sea flux, which responds to the decrease of DIC due to precipitation and to the cooling effect that increases the solubility of carbon in seawater, yields a net ocean uptake (see the histogram), although east of several major topographic features there is outgassing. F_{CO_2} , *BIO*, *DIFF*, and *DILUT* almost balance each other. Thus, the net *TEND* (black bar in the histogram) is mostly driven by the ocean circulation.

In winter, the net *BIO* term (histogram) is negligible with respect to the other terms, as remineralization in the east Indian Ocean and in the Pacific sector is balanced by production occurring elsewhere. Again, *DILUT* (evaporation and precipitation) and air-sea CO₂ flux vary strongly with longitude, and drive opposite net effects, with *DILUT* decreasing the DIC concentration and air-sea CO₂ flux increasing it. The spatial pattern for the F_{CO_2} term shows a large uptake in the Indian Ocean sector and outgassing in the central Pacific. Overall, *ADV*, F_{CO_2} , and *DIFF* together drive a net uptake of DIC in winter.

Thus, the carbon budget balance in the ACC is strongly dependent on season and location. Two factors most important to the budget are (1) the large-scale upwelling and the northward Ekman transport of carbon-rich waters, which determine the largest input of carbon to the budget, and (2) topographic interaction, which sets hot spots where biological production is large. The change in DIC due to dilution and air-sea CO₂ exchange are strongly variable with the location. Dilution acts as a constant sink of carbon in the ACC waters, while air-sea CO₂ fluxes mostly drive a net ocean uptake, except in summer. In general, the spatial and temporal variability of the air-sea CO₂ flux is determined by the *DILUT* term, the biological sink, and temperature changes (which affect the solubility).

3.5.2.2. Subtropical Region

The depth and time average of the DIC budget terms, integrated in latitude for the region north of the ACC to 26.6°S, are shown in Figure 10. The divergence of DIC advection decreases the DIC concentration almost everywhere due to downwelling (Figure 4a), with the exception being in the southeast Pacific and in some regions close to topography, where the mean geostrophic and ageostrophic advection terms (Figures 4c and 4f) supply DIC. However, unlike the ACC region, where the circulation dominates over the other processes, here the *TEND* is modulated by various mechanisms.

In the eastern Atlantic sector biological uptake occurs in the coastal upwelling system of the Benguela current (~15°E) along the west coast of Africa (Figure 4a) where nutrient supply triggers primary productivity [Boyer *et al.*, 2000] from winter to summer (Figure 11). In this region, the flux of CO₂ is positive in each season (Figure 11). The net ocean uptake is mainly driven by the drawdown of CO₂ due to biology, as observed also by González-Dávila *et al.* [2009] and Santana-Casiano *et al.* [2009]. This is also a region of net

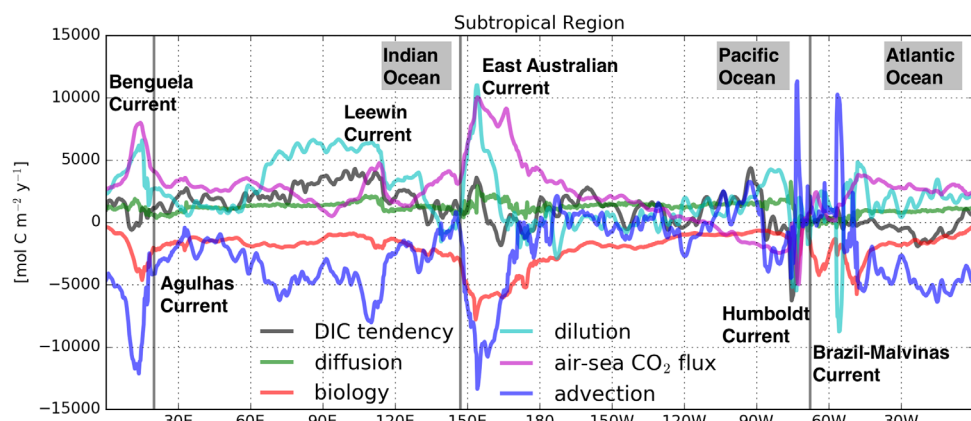


Figure 10. Temporal mean (5 years) of the DIC budget terms in the subtropical region, vertically averaged over depth (0–650 m) and integrated over latitude (from the northern limit of the ACC band up to 26.6°S). The DIC tendency (black) is the sum of all terms: divergence of advective transport (blue), diffusive transport (green), biological processes (red), air-sea flux (magenta), and freshwater flux (cyan).

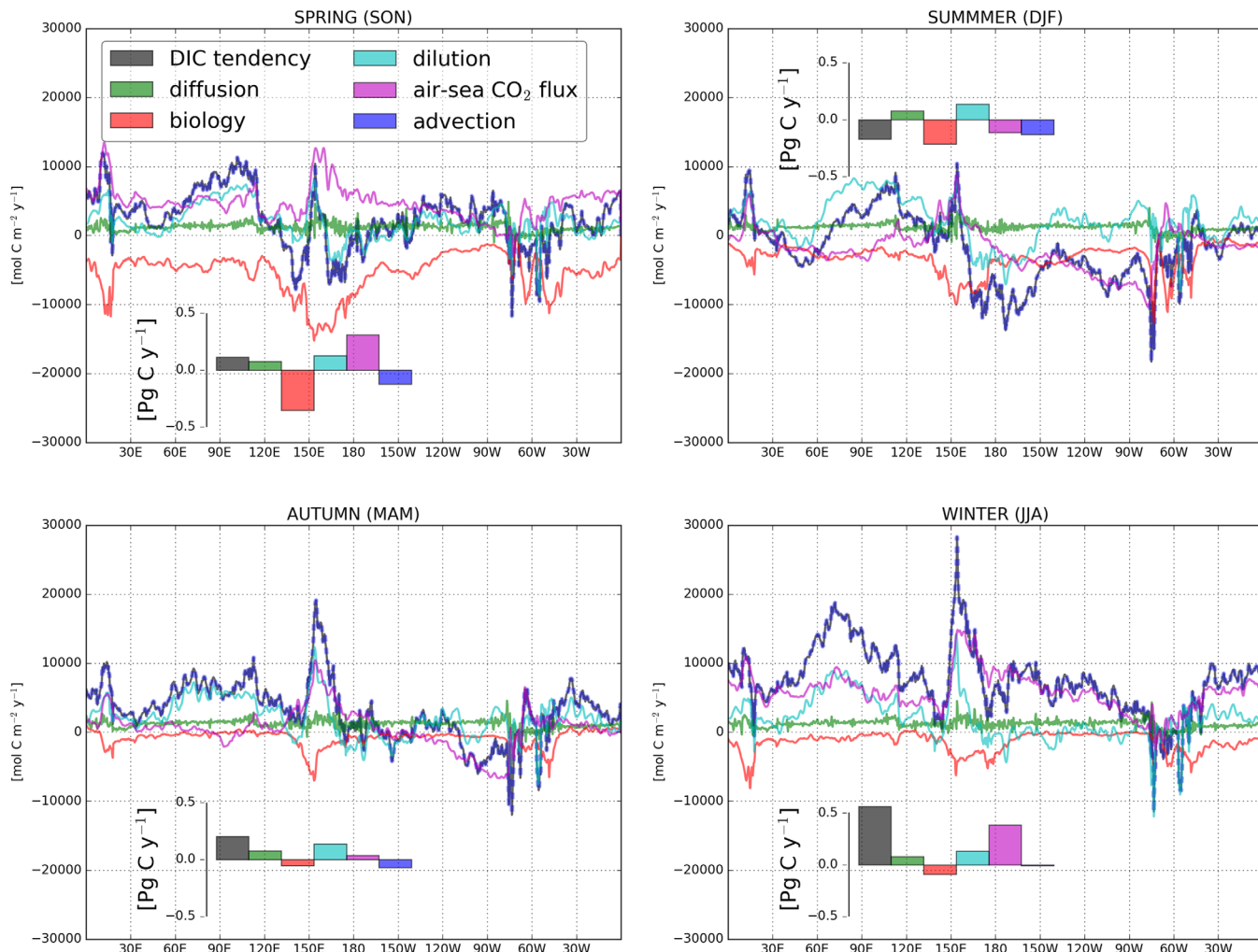


Figure 11. Same as Figure 9, but for the subtropical region.

evaporation, which increases the DIC concentration in each season and, together with F_{CO_2} , drives the seasonal material derivative of DIC.

In the western Atlantic sector, the Brazil-Malvinas confluence (east of 70°W) is one of the most productive areas in the Southern Hemisphere [Moore and Abbott, 2000], and consequently one of the major locations of carbon uptake [Feely *et al.*, 2001; Bianchi *et al.*, 2009]. Our results show evidence of this process (Figures 10 and 11), in particular in warmer months. Another striking feature in this area is the large input from Rio de la Plata, at approximately 35°S, 55°W (Figure 3e): at this location, *DILUT* balances the supply due to advection of DIC driven by upwelling and geostrophic anomaly (Figures 4a and 4d, respectively).

In the central Atlantic sector, the large drawdown of carbon due to the circulation (Figure 10) is a signature of downwelling (Figure 4a). Biological productivity occurs in each season except autumn, where remineralization drives a small supply of DIC. The biological sink of DIC is particularly large in spring, where it drives air-sea CO₂ flux into the ocean. Conversely, in winter the carbon flux is impacted by solubility, which increases when temperature decreases. A net evaporation explains the overall effect of the *DILUT* term.

In the Indian Ocean, the advective divergence draws down the DIC concentration, particularly in the warm, poleward flowing Leewin Current system west of Australia and in the region south of Australia. The low productivity of the Leewin Current is typical of a nutrient-poor environment lacking of upwelling (Figure 10). However, we do not find the expected enhancement of productivity (Figure 11) in winter and fall [e.g., Koslow *et al.*, 2008], possibly due to the lack of resolved mesoscale structures in the model, which are known to

contribute to nutrient delivery in this area [Koslow *et al.*, 2008]. Around Tasmania, approximately between 140°E–160°E, biological productivity drives CO₂ uptake in each season. This is the most productive area of the subtropical region and also a region of large variability in evaporation and dilution processes (Figure 11).

The southeast Pacific site of deep winter mixed layers [Hanawa and Talley, 2001] shows a net increase of DIC (Figure 10), where input of carbon due to air-sea CO₂ flux is as large as the export driven by downwelling of surface waters. Large peaks of positive *TEND* are concentrated in the eastern region, west of the Humboldt Current (between Chile and Peru, around 75°W). The Humboldt Current is a highly productive area [Moore and Abbott, 2000], which drives carbon uptake in spring (Figure 11). At this location, the large upwelling (Figures 4a and 4b) and mean ageostrophic advection (Figure 4e) contrast the drawdown of DIC driven by biology and, on average, drive a net outgassing of CO₂ (Figure 10). The seasonal budget of the southeast Pacific (Figure 11) indicates that both *BIO*, *F_{CO₂}*, and *DILUT* drive the variability and the pattern of the material derivative.

Overall, we find a small net DIC increase throughout the year, except during summer (inset in Figure 11). In spring, air-sea CO₂ fluxes are driven and balanced by biological production, while carbon export due to *ADV* is in part balanced by evaporation. In summer, DIC decreases due to the combination of biological production, outgassing and export of DIC by ocean circulation, which are partly compensated by mixing and evaporation. In locations where biological production is small (between southeast Africa and Australia, and between New Zealand and South America), the reduced solubility due to warmer temperatures dominates the response in CO₂ flux. The resulting outgassing in these regions is larger than the uptake occurring elsewhere. In autumn, all mechanisms except *ADV* and *BIO* increase the DIC concentration. In this season, the air-sea CO₂ flux is largely balanced by biological production, while export by ocean circulation partly compensates the impact of the evaporation and mixing. The largest increase in DIC is observed in winter, due to a combination of mixing, evaporation, and large air-sea CO₂ flux driven by both biological productivity and cooling.

3.5.2.3. Antarctic Region

The DIC budget for the Antarctic region, which is computed for the area extending from 78°S up to the southern ACC boundary, is shown as a 5 year mean in Figure 12 and as seasonal means in Figure 13. In this region, the tendency of DIC is almost everywhere positive (Figure 12). *ADV* and *DILUT* are the largest terms in the carbon budget and mostly compensate each other (Figure 12). These terms are strongly variable at all longitudes, and present larger peaks in the Prydz Bay Amery ice shelf, west of the Ross Gyre, east of the Amundsen Sea, and west of the Weddell Gyre, locations of large sea ice formation and export. In particular, geostrophic advection, which is responsible for the export of carbon in the western side of the cyclonic Prydz Bay, Ross and Weddell gyres (Figures 3 and 4d, and 4f), is compensated by carbon dilution due to freshwater redistribution by sea ice in these locations (*DILUT* term in Figure 12). In addition to the effects of

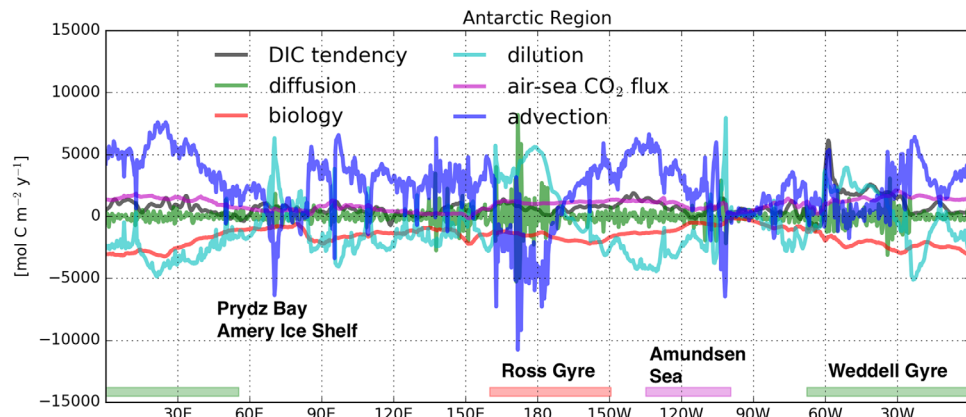


Figure 12. Time mean (5 years) of the DIC budget terms in the Antarctic region, vertically averaged over depth (0–650 m) and integrated over latitude (from the model southern boundary to the edge of the southern limit of the ACC band). The DIC tendency (black) is the sum of all terms: divergence of advective transport (blue), diffusive transport (green), biological processes (red), air-sea flux (magenta), and freshwater flux (cyan).

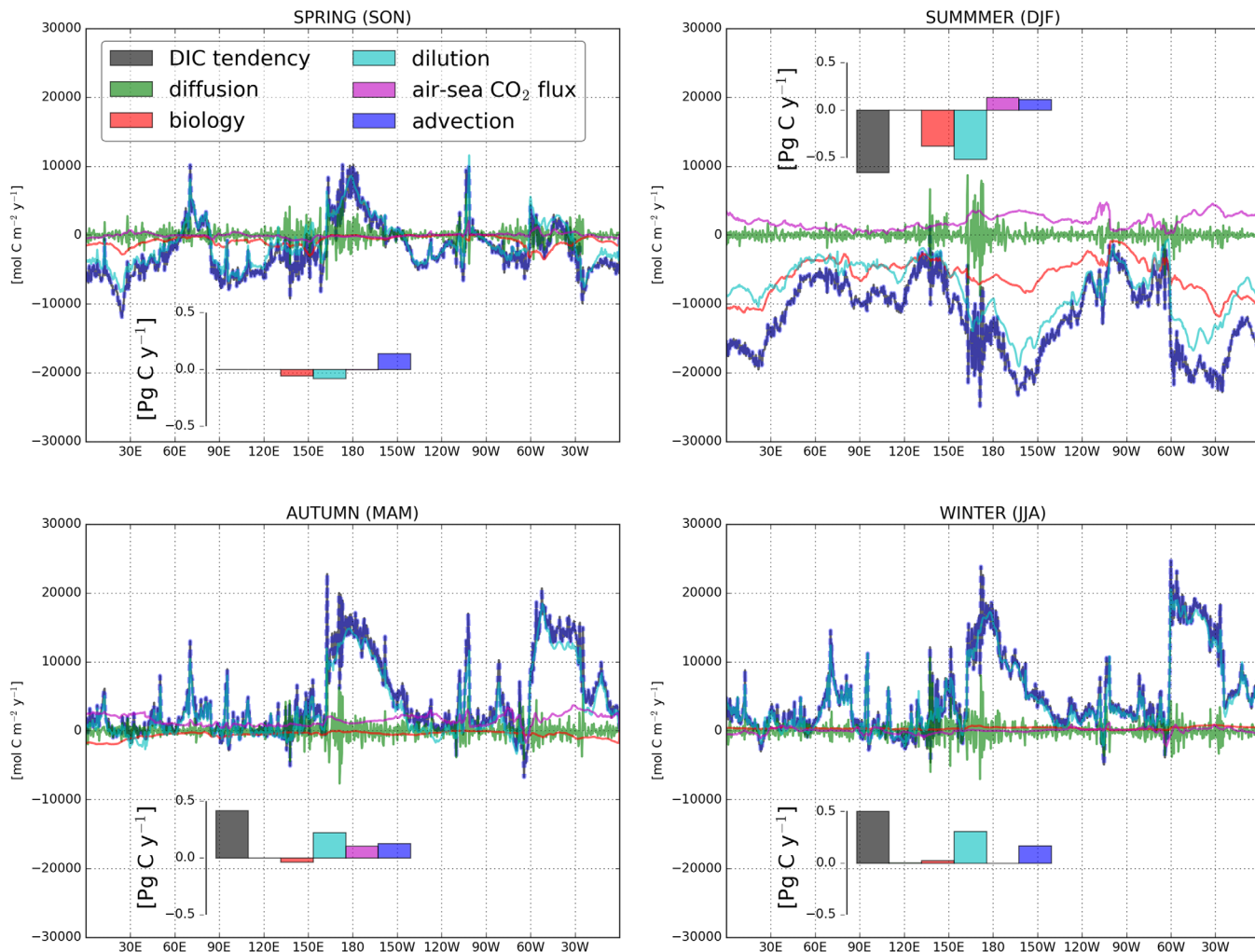


Figure 13. Same as Figure 9, but for the Antarctic region.

ADV and *DILUT*, the DIC concentration is affected by a net CO₂ ingassing, which is modulated by the biological term. Mixing due to horizontal processes over the continental shelf is highly variable, with large values in the Ross Gyre. The histograms in Figure 13 reveal, however, that the net contribution of mixing is negligible.

We find that in spring (Figure 13) the sum of the biological sink and the reduced DIC concentration due to sea ice melt and runoff balances the net increase due to ocean circulation, *ADV*. The air-sea CO₂ flux is negligible, as regions of small ingassing responding to biological production are compensated by areas of outgassing. There is a net dilution in these months due to the onset of sea ice melt in the Weddell Gyre and in the eastern part of the Ross Gyre. In the western Ross Gyre (around 180°) sea ice melt, and hence dilution, are delayed until summer [Arrigo *et al.*, 1998].

Summer shows the largest DIC sink, where the change in the DIC material derivative is driven by the decrease in DIC concentration due to sea ice melt (Figure 13) and biological production. Due to warmer temperatures, the solubility pump favors outgassing. However, the air-sea CO₂ flux is reversed, as a net uptake arises to balance the carbon export due to biological production and dilution.

In autumn the DIC material derivative is largely driven by *DILUT*, which mostly reflects sea ice formation. The spatial variability of the air-sea CO₂ flux reflects the variability in the biological term, which is significant in the Weddell Gyre and negligible in most other regions. In this season solubility increases as temperatures decrease, promoting a net ingassing.

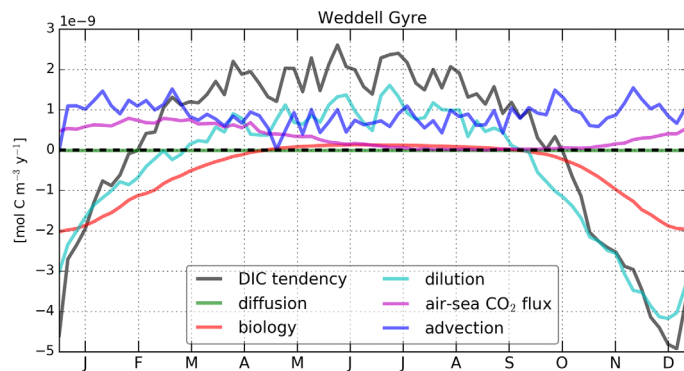


Figure 14. Volume average of the seasonal Weddell Gyre DIC budget. The DIC tendency (black) is the sum of all terms: divergence of advective transport (blue), diffusive transport (green), biological processes (red), air-sea flux (magenta), and fresh-water flux (cyan).

Ocean circulation and sea ice processes are the main players in the carbon budget of the Antarctic region. Biology is important in warmer months as increased light availability, together with shoaling mixed layers due to sea ice melt, triggers production [Lancelot *et al.*, 1993]. Sea ice export, biological activity, and supply/export of DIC due to the circulation then drive a response in air-sea CO_2 flux.

3.5.2.4. The Weddell Gyre

We conclude the results section by exploring in more detail the Weddell Gyre carbon budget, as this is a largely undocumented and important regional component of the climate system. Figure 14 shows the volume average annual cycle of the Weddell Gyre carbon budget. ADV is strongly reduced in the gyre integral, compared to the regional budgets shown in the previous sections. Here the circulation increases carbon at a mean rate of $\sim 1 \text{ mol C m}^{-3} \text{ yr}^{-1}$. In spring and summer the tendency of DIC is driven by sea ice and snow melt and biological production, consequently resulting in an uptake of CO_2 from air-sea fluxes. During the rest of the year, $TEND$ is mainly regulated by ocean circulation and sea ice production and runoff: as the formation of sea ice takes place (March–mid-September), air-sea CO_2 flux is reduced and become negligible around winter.

4. Discussion and Conclusions

This work represents the first diagnosis of the upper ocean (top 650 m) DIC budget in a physical-biogeochemical state estimate of Southern Ocean. We investigate the impact of the various drivers of temporal change of DIC in three subdomains of the Southern Ocean, namely the ACC, the subtropics, and the Antarctic regions (see Figure 1), and provide an estimate of the relative impact of each process over different temporal scales. Because the model does not resolve small-scale structures, the focus is limited to large-scale processes.

We have found that the circulation, specifically the divergence of the advective flux, ADV (Figure 3), represents the largest factor contributing to the tendency of DIC in every location of the Southern Ocean (Figures 8 and 13) and explains most of the variance of the tendency of DIC at all temporal scales. Locally, the effect of the circulation on the temporal change of DIC is determined by both horizontal and vertical processes from both ageostrophic and geostrophic velocities (Figures 3a and 4). The large-scale overturning circulation is apparent, with significant DIC increase in wind-driven upwelling regions and subduction in the subtropical wind-driven downwelling regions. The northward Ekman transport over the ACC is influential. In the regional integral the net budget (Figure 15) shows that it is the vertical overturning component of ADV (vertical hatch) that dominates the advective supply/export of DIC. Nevertheless, in the boundary currents the net reduction of DIC (Figure 3) is due to the export by the geostrophic component. However, advection is a redistribution and not a sink or source, and thus the contribution of the advective flux is strongly reduced by volume-averaging over the whole Southern Ocean (Figure 7) or regionally (Figures 14 and 15).

The hot spots of larger variability of the tendency (Figure 2d) are driven by diffusive processes at frequencies shorter than 45 days (Figure 6a). Furthermore, at any temporal scale $DIFF$ is important in localized spots,

Due to the increase in sea ice cover during winter, air-sea CO_2 flux and BIO , which reflects small net remineralization processes, are strongly reduced and their contribution to the change in DIC is negligible. Sea ice formation commences in the Weddell Gyre and continues in the Ross Gyre. Sea ice processes, together with DIC supply due to ocean circulation and remineralization, drive a net increase in DIC.

In the Antarctic region, as in the ACC and in the subtropics, the processes that control the DIC concentration are locally and temporally variable.

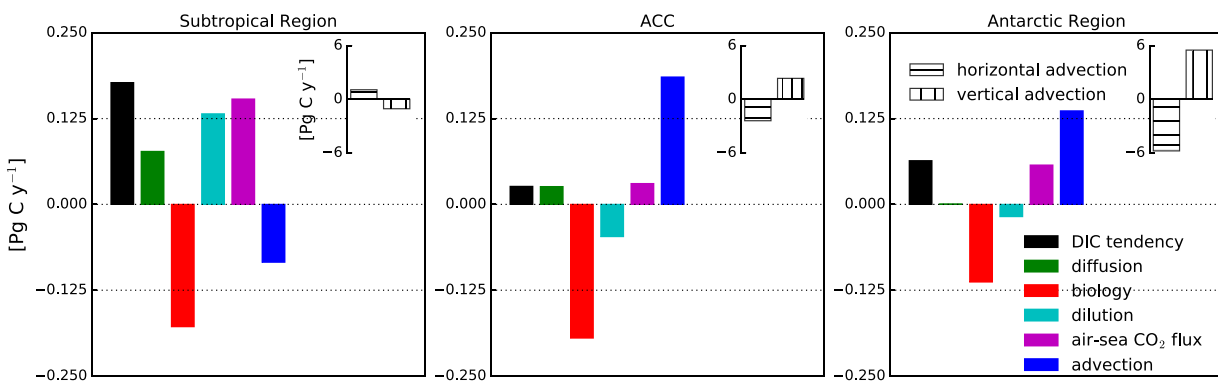


Figure 15. Net spatial and time integral of each term of the DIC budget, plotted for (a) subtropical region, (b) ACC, and (c) Antarctic region. Color code as in Figure 7 and listed in Figure 15c. The ADV term (blue) has been divided into horizontal (ADV_h) and vertical (ADV_z) components (embedded frames): ADV_h , and ADV_z are identified by horizontal and vertical hatches, respectively.

such as over the continental shelf, downstream of topographic features and in regions of meandering fronts. On average, instead, the diffusive term contributes with a large net input to the DIC increase only in the subtropical region, while it is strongly reduced in the ACC and is negligible elsewhere (Figure 15).

Biological processes are important for DIC changes near topographic features (Figure 8), in boundary currents (Figure 10) and in the marginal sea ice zone (Figure 12). Biological production acts as a sink of DIC generally during warmer months, and it is a strong component of the DIC budget throughout the whole year in the very productive areas around Tasmania and in the Benguela and Humboldt Currents (Figures 3c and 11). At timescales shorter than 45 days, this term explains the variability of the change of DIC only over the continental shelf (Figure 5b). Off the shelf it becomes more important at longer timescales. Finally, on average, *BIO* represents a net sink of carbon in every region (Figure 15).

The variability of DIC is also influenced by the air-sea CO₂ exchange, which is a direct consequence of the difference of carbon pressure at the interface between seawater and air. B-SOSE shows a predominant uptake of carbon in each region (Figure 15), in part induced by the increase in atmospheric CO₂. The large-scale mean CO₂ flux patterns (Figure 3d) compare well with *Takahashi et al.* [2009, Figure 13], in the ACC and in the subtropical region. However, we do not find net outgassing in the Antarctic region, as in *Takahashi et al.* [2009], which could be due to, other than a model bias, a different time span between that product and our model. The lack in year-round observations outside the Drake Passage prevents assessment as to which product is more accurate.

The net ocean uptake of carbon via surface air-sea CO₂ flux locally occurs to balance the advective transport, the biological sink, and/or the dilution of carbon concentration due to precipitation, runoff and sea ice melt (Figures 8–14 and 15). Nevertheless, the variability in time and space of the CO₂ flux is very large, and, though net carbon outgassing does not stand out in our mean state, it does in several locations and time scales: for example, (1) in the ACC we find larger peaks of outgassing at localized spots in all the three ocean sectors (Figure 9); (2) outgassing occurs in summer over the subtropical region except in locations where biological production is large, and it also occurs in autumn in the Pacific sector (Figure 11). However, we do not find any net outgassing in the Antarctic region (Figures 13–14). The float-based estimates of CO₂ flux by A. Gray and J. Sarmiento (personal communication, 2017) infer outgassing in the ACC and subtropical areas, as we did, but they also find outgassing in the Antarctic region, which is not present in our analysis. The large variability of this region, which has been also highlighted by A. Gray and J. Sarmiento (personal communication, 2017), may be a cause of this discrepancy. Because of this variability, it is nontrivial to compare point flux estimates with our spatially integrated values. Validation of the spatiotemporal variability we have hypothesized in this work will be facilitated with increased observational coverage.

Finally, *DILUT* is a leading mechanism in driving the tendency of DIC south of approximately 50°S at all temporal scales (Figure 5d), and influences both biological processes and air-sea CO₂ flux (Figure 12). In the subtropical zone, *DILUT* is important over interannual scales, where it drives a net increase of carbon (Figure 15) reflecting the excess of evaporation over precipitation and river runoff. Elsewhere, on average precipitation and sea ice export and melting reduce the DIC concentration (Figure 15).

In conclusion, the DIC budget in the Southern Ocean is regulated by a complex interaction of ocean transport, biological processes, air-sea exchange, sea ice mechanisms and mixing. The importance of each term depends on the time and space scales considered. Transport dominates the local impact, but can be reduced by spatial averaging. Diagnosing locations of greatest variability of DIC concentration, such as the ACC, the Malvinas Current, the Agulhas Current region, and east of Tasmania, is beneficial to both planning an observing system and drawing inferences from observations. By providing information on the scales of variability of the different drivers, the present work informs the carbon cycle which is presently inferred from sparse observations.

Appendix A: Comparison of B-SOSE With a Forward Model

An unoptimized $1/3^{\circ}$ resolution forward simulation was developed prior to B-SOSE. The model was forced by atmosphere reanalysis alone (the global atmospheric ECMWF ERA-interim reanalysis of *Dee et al.* [2011]), spun up for 3 years, and then integrated between 2005 and 2014, with a time step of 1 h. Physical and biogeochemical configurations of the nonoptimized model were the same as in B-SOSE (see section 2 and Table 1).

An analysis of the mean state of the forward model has been conducted and the results (which are not shown here for brevity) compared to B-SOSE. This comparison has revealed several differences, which highlights the improvement of the optimization. B-SOSE is the result of 105 iterations of the adjoint method, and at every iteration the model-observation misfit is reduced and the consistency of the output to the data is improved [*Verdy and Mazloff*, 2017]. The differences between the two simulations (B-SOSE versus the forward model) can be used to explore how optimization has changed the solution. In particular, differences are found in both the ocean circulation and the carbon system and are listed here:

1. Both models show a trend in the DIC concentration, but there is a significant reduction of the trend in the state estimate.
2. The divergence of the advective transport of DIC in B-SOSE has a larger spatial variability, as the ocean data have informed structures in the flow that were absent in the forward model.
3. Both remineralization and biological production are reduced with the optimization, especially remineralization in the subtropical area, and production in the ACC and subtropics.
4. The optimized air-sea CO_2 uptake is strongly reduced in several locations, such as around Tasmania, the Malvinas Current, in the subtropical Pacific, and in the ACC, where we also noticed the major differences in the biological term; also, there are several locations of outgassing in each basin in the ACC (discussed in the previous sections), which were absent in the forward run;
5. The optimization reduced the freshwater flux everywhere in the Southern Ocean, and areas of net evaporation in the ACC emerged, which were not present in the forward run.

Despite the local differences, the integrated mean air-sea CO_2 flux south of 44°S does not substantially differ in the two simulations. The models show in fact a mean uptake of $0.17 \text{ Pg C yr}^{-1}$ (forward run) and $0.18 \text{ Pg C yr}^{-1}$ (B-SOSE), which fit within the estimates of *Gruber et al.* [2009] ($0.34 \pm 0.20 \text{ Pg C yr}^{-1}$) and *Takahashi et al.* [2009] ($0.30 \pm 0.17 \text{ Pg C yr}^{-1}$).

B-SOSE still has problematic regions; a few biases have been identified in the upper ocean [*Verdy and Mazloff*, 2017]. These biases likely result from model error, and may be reduced by improving the model physics and representation of biogeochemistry. Increasing observations of nutrients and the carbon components (i.e., DIC, alkalinity and pH) will reveal how to improve the model solution. Observations from the autonomous floats of the SOCCOM project (<https://soccom.princeton.edu/>) or the repeated hydrographic sections of the Global Ocean Ship-Based Hydrographic Investigations Program [*Talley et al.*, 2016] can provide these constraints. Despite remaining issues suspected in B-SOSE, the fit with observations is satisfactory in many regions [*Verdy and Mazloff*, 2017], which emphasizes the benefit of the optimization method. B-SOSE reveals structures of the circulation that were absent in the forward model, and we expect changes in the carbon cycle are better represented.

Acknowledgments

This work is a contribution of the Southern Ocean Carbon and Climate Observations and Modeling project (SOCCOM). SOCCOM is supported by the National Science Foundation under NSF award PLR-1425989. B-SOSE output is available at <http://sose.ucsd.edu>.

References

- Abernathay, R. P., I. Cerovecki, P. R. Holland, E. Newsom, M. Mazloff, and L. D. Talley (2016), Water-mass transformation by sea ice in the upper branch of the Southern Ocean overturning, *Nat. Geosci.*, 9(8), 596–601. doi:10.1038/ngeo2749.
Abraham, E. R., C. S. Law, P. W. Boyd, S. J. Lavender, M. T. Maldonado, and A. R. Bowie (2000), Importance of stirring in the development of an iron-fertilized phytoplankton bloom, *Nature*, 407(6805), 727–730.

- Adcroft, A., C. Hill, and J. Marshall (1997), Representation of topography by shaved cells in a height coordinate ocean model, *Mon. Weather Rev.*, 125(9), 2293–2315.
- Amante, C., and B. W. Eakins (2009), ETOPO1 Global Relief Model converted to PanMap layer format, NOAA-National Geophysical Data Center, PANGAEA, doi:10.1594/PANGAEA.769615.
- Arrigo, K. R., and G. L. van Dijken (2004), Annual changes in sea-ice, chlorophyll *a*, and primary production in the Ross Sea, Antarctica, *Deep Sea Res. Part II*, 51(1), 117–138.
- Arrigo, K. R., A. M. Weiss, and W. O. Smith (1998), Physical forcing of phytoplankton dynamics in the southwestern Ross Sea, *J. Geophys. Res.*, 103(C1), 1007–1021.
- Bakker, D. (2014), An update to the surface ocean CO₂ atlas (SOCAT version 2), *Earth Syst. Sci. Data*, 6, 69–90.
- Bakker, D. (2016), A multi-decade record of high quality fCO₂ data in version 3 of the surface ocean CO₂ atlas (SOCAT version 2), *Earth Syst. Sci. Data*, 8(2), 383–413, doi:10.5194/essd-2016-15.
- Bakker, D., H. De Baar, and U. Bathmann (1997), Changes of carbon dioxide in surface waters during spring in the Southern Ocean, *Deep Sea Res. Part II*, 44(1), 91–127.
- Bianchi, A. A., D. R. Pino, H. G. I. Perlenler, A. P. Osiroff, V. Segura, V. Lutz, M. L. Clara, C. F. Balestrini, and A. R. Piola (2009), Annual balance and seasonal variability of sea-air CO₂ fluxes in the Patagonia Sea: Their relationship with fronts and chlorophyll distribution, *J. Geophys. Res.*, 114, C03018, doi:10.1029/2008JC004854.
- Blain, S., et al. (2007), Effect of natural iron fertilization on carbon sequestration in the Southern Ocean, *Nature*, 446, 1070–1074.
- Bowie, A. R., et al. (2015), Iron budgets for three distinct biogeochemical sites around the Kerguelen archipelago (Southern Ocean) during the natural fertilisation experiment KEOPS-2, *Biogeosciences*, 12, 4421–4445.
- Boyd, P. W., et al. (2000), A mesoscale phytoplankton bloom in the polar Southern Ocean stimulated by iron fertilization, *Nature*, 407(6805), 695–702.
- Boyer, D., J. Cole, and C. Bartholomae (2000), Southwestern Africa: Northern Benguela current region, *Mar. Pollut. Bull.*, 1(41), 123–140.
- Carranza, M. M., and S. T. Gille (2015), Southern Ocean wind-driven entrainment enhances satellite chlorophyll-*a* through the summer, *J. Geophys. Res. Oceans*, 120, 304–323, doi:10.1002/2014JC010203.
- Cerovečki, I., L. D. Talley, M. R. Mazloff, and G. Maze (2013), Subantarctic mode water formation, destruction, and export in the eddy-permitting Southern Ocean state estimate, *J. Phys. Oceanogr.*, 43(7), 1485–1511.
- Chelton, D., R. DeSzoeke, M. Schlax, K. El Naggar, and N. Siwertz (1998), Geographical variability of the first baroclinic Rossby radius of deformation, *J. Phys. Oceanogr.*, 28, 433–460.
- Chelton, D. B., M. G. Schlax, D. L. Witter, and J. G. Richman (1990), Geosat altimeter observations of the surface circulation of the Southern Ocean, *J. Geophys. Res.*, 95(C10), 17,877–17,903.
- Chever, F., G. Sarthou, E. Bucciarelli, S. Blain, and A. R. Bowie (2010), An iron budget during the natural iron fertilisation experiment KEOPS (Kerguelen Islands, Southern Ocean), *Biogeosciences*, 7, 455–468.
- Coale, K. H., et al. (2004), Southern Ocean iron enrichment experiment: Carbon cycling in high- and low-Si waters, *Science*, 304(5669), 408–414.
- Dai, A., and K. E. Trenberth (2002), Estimates of freshwater discharge from continents: Latitudinal and seasonal variations, *J. Hydrometeorol.*, 3(6), 660–687.
- de Baar, H. J., A. G. Buma, R. F. Nolting, G. C. Cadée, G. Jacques, and P. J. Tréguer (1990), On iron limitation of the Southern Ocean: Experimental observations in the Weddell and Scotia Seas, *Mar. Ecol. Prog. Ser.*, 65, 105–122.
- Dee, D., et al. (2011), The ERA-Interim reanalysis: Configuration and performance of the data assimilation system, *Q. J. R. Meteorol. Soc.*, 137(656), 553–597.
- Dunne, J. P., R. A. Armstrong, A. Gnanadesikan, and J. L. Sarmiento (2005), Empirical and mechanistic models for the particle export ratio, *Global Biogeochem. Cycles*, 19, GB4026, doi:10.1029/2004GB002390.
- Eppley, R. W. (1972), Temperature and phytoplankton growth in the sea, *Fishery Bull.*, 70(4), 1063–1085.
- Fay, A., and G. McKinley (2013), Global trends in surface ocean pCO₂ from in situ data, *Global Biogeochem. Cycles*, 27, 541–557, doi:10.1002/gbc.20051.
- Fay, A. R., G. A. McKinley, and N. S. Lovenduski (2014), Southern Ocean carbon trends: Sensitivity to methods, *Geophys. Res. Lett.*, 41, 6833–6840.
- Feely, R. A., C. L. Sabine, T. Takahashi, and R. Wanninkhof (2001), Uptake and storage of carbon dioxide in the ocean: The global CO₂ survey, *Oceanography*, 14(4), 18–32.
- Fenty, I., and P. Heimbach (2013), Hydrographic preconditioning for seasonal sea ice anomalies in the Labrador Sea, *J. Phys. Oceanogr.*, 43(5), 863–883.
- Forget, G., J.-M. Campin, P. Heimbach, C. Hill, R. Ponte, and C. Wunsch (2015), ECCO version 4: An integrated framework for non-linear inverse modeling and global ocean state estimation, *Geosci. Model Dev.*, 8, 3071–3104.
- Galbraith, E. D., A. Gnanadesikan, J. P. Dunne, and M. R. Hiscock (2010), Regional impacts of iron-light colimitation in a global biogeochemical model, in *Proceedings From the 2010 AGU Ocean Sciences Meeting*, AGU, Washington, D. C.
- Garcia, H. E., R. A. Locarnini, T. P. Boyer, J. I. Antonov, O. Baranova, M. M. Zweng, J. R. Reagan, and D. R. Johnson (2014a), World ocean atlas 2013 volume 3: Dissolved oxygen, apparent oxygen utilization, and oxygen saturation, *NOAA Atlas NESDIS* 75, p. 27.
- Garcia, H. E., R. A. Locarnini, T. P. Boyer, J. I. Antonov, O. Baranova, M. M. Zweng, J. R. Reagan, and D. R. Johnson (2014b), World ocean atlas 2013, volume 4: Dissolved inorganic nutrients (phosphate, nitrate, silicate), *NOAA Atlas NESDIS* 76, p. 25.
- Gille, S. T., M. M. Carranza, R. Cambra, and R. Morrow (2014), Wind-induced upwelling in the Kerguelen Plateau region, *Biogeosciences*, 11(22), 6389–6400, doi:10.5194/bg-11-6389-2014.
- González-Dávila, M., J. M. Santana-Casiano, and I. R. Ucha (2009), Seasonal variability of fCO₂ in the Angola-Benguela region, *Prog. Oceanogr.*, 83(1–4), 124–133, doi:10.1016/j.pocean.2009.07.033.
- Gould, J., et al. (2004), Argo profiling floats bring new era of in situ ocean observations, *Eos Trans. AGU*, 85(19), 179–184.
- Gruber, N., et al. (2009), Oceanic sources, sinks, and transport of atmospheric CO₂, *Global Biogeochemical Cycles*, 23, GB1005, doi:10.1029/2008GB003349.
- Hammond, M. D., and D. C. Jones (2017), Freshwater flux from ice sheet melting and iceberg calving in the Southern Ocean, *Geosci. Data J.*, 3: 60–62. doi:10.1002/gdj3.43.
- Hanawa, K., and L. D. Talley (2001), Mode waters, in *Ocean Circulation and Climate*, Int. Geophys. Ser., edited by G. Siedler et al., pp. 373–386, Academic Press, San Diego, Calif.
- Ito, T., J. Marshall, and M. Follows (2004), What controls the uptake of transient tracers in the Southern Ocean?, *Global Biogeochem. Cycles*, 18, GB2021, doi:10.1029/2003GB002103.
- Jouandet, M. P., S. Blain, N. Metzl, C. Brunet, T. W. Trull, and I. Obernosterer (2008), A seasonal carbon budget for a naturally iron-fertilized bloom over the Kerguelen Plateau in the Southern Ocean, *Deep Sea Res. Part II*, 55(5), 856–867.

- Key, R. M., et al. (2015), Global ocean data analysis project, version 2 (GLODAPv2), ORNL/CDIAC-159, NDP-093, Carbon Dioxide Inf. Anal. Cent. Oak Ridge Natl. Lab., US Dep. Energy, Oak Ridge, Tenn., doi:10.3334/CDIAC/OTG.NDP093_GLODAPv2.
- Khatiwala, S., F. Primeau, and T. Hall (2009), Reconstruction of the history of anthropogenic CO₂ concentrations in the ocean, *Nature*, 462(7271), 346–349.
- Koslow, J. A., S. Pesant, M. Feng, A. Pearce, P. Fearn, T. Moore, R. Matear, and A. Waite (2008), The effect of the Leeuwin Current on phytoplankton biomass and production off Southwestern Australia, *J. Geophys. Res.*, 113, C07050, doi:10.1029/2007JC004102.
- Lancelot, C., S. Mathot, C. Veth, and H. de Baar (1993), Factors controlling phytoplankton ice-edge blooms in the marginal ice-zone of the northwestern Weddell Sea during sea ice retreat 1988: Field observations and mathematical modelling, *Polar Biol.*, 13(6), 377–387.
- Landschützer, P., N. Gruber, D. Bakker, and U. Schuster (2014), Recent variability of the global ocean carbon sink, *Global Biogeochem. Cycles*, 28(9), 927–949.
- Landschützer, P., et al. (2015), The reinvigoration of the Southern Ocean carbon sink, *Science*, 349(6253), 1221–1224.
- Large, W., and S. Yeager (2009), The global climatology of an interannually varying air-sea flux data set, *Clim. Dyn.*, 33(2–3), 341–364.
- Lauvset, S. K., et al. (2016), A new global interior ocean mapped climatology: The 1° × 1° GLODAP version 2, *Earth Syst. Sci. Data Discuss.*, 8(2), 325–340, doi:10.5194/esd-2015-43.
- Le Quéré, C., et al. (2009), Trends in the sources and sinks of carbon dioxide, *Nat. Geosci.*, 2(12), 831–836.
- Lenton, A., N. Metz, T. Takahashi, M. Kuchinke, R. J. Matear, T. Roy, S. C. Sutherland, C. Sweeney, and B. Tilbrook (2012), The observed evolution of oceanic pCO₂ and its drivers over the last two decades, *Global Biogeochem. Cycles*, 26, GB2021, doi:10.1029/2011GB004095.
- Losch, M., D. Menemenlis, J.-M. Campin, P. Heimbach, and C. Hill (2010), On the formulation of sea-ice models: Part 1: Effects of different solver implementations and parameterizations, *Ocean Modell.*, 33(1), 129–144.
- Lovenduski, N. S., N. Gruber, and S. C. Doney (2008), Toward a mechanistic understanding of the decadal trends in the Southern Ocean carbon sink, *Global Biogeochem. Cycles*, 22, GB3016, doi:10.1029/2007GB003139.
- Mahowald, N. M., A. R. Baker, G. Bergametti, N. Brooks, R. A. Duce, T. D. Jickells, N. Kubilay, J. M. Prospero, and I. Tegen (2005), Atmospheric global dust cycle and iron inputs to the ocean, *Global Biogeochem. Cycles*, 19, GB4025, doi:10.1029/2004GB002402.
- Marshall, J., and K. Speer (2012), Closure of the meridional overturning circulation through Southern Ocean upwelling, *Nat. Geosci.*, 5(3), 171–180.
- Marshall, J., A. Adcroft, C. Hill, L. Perelman, and C. Heisey (1997), A finite-volume, incompressible Navier Stokes model for studies of the ocean on parallel computers, *J. Geophys. Res.*, 102(C3), 5753–5766.
- Martin, J. H. (1990), Glacial-interglacial CO₂ change: The iron hypothesis, *Paleoceanography*, 5(1), 1–13.
- Masich, J., T. K. Chereskin, and M. R. Mazloff (2015), Topographic form stress in the Southern Ocean state estimate, *J. Geophys. Res. Oceans*, 120, 7919–7933, doi:10.1002/2015JC011143.
- Mazloff, M. R., P. Heimbach, and C. Wunsch (2010), An eddy-permitting Southern Ocean state estimate, *J. Phys. Oceanogr.*, 40(5), 880–899.
- McKinley, G. A., A. R. Fay, N. S. Lovenduski, and D. J. Pilcher (2017), Natural variability and anthropogenic trends in the ocean carbon sink, *Annu. Rev. Mar. Sci.*, 9, 125–150.
- Meier, W., F. Fetterer, M. Savoie, S. Mallory, R. Duerr, and J. Stroeve (2016), NOAA/NSIDC climate data record of passive microwave sea ice concentration, version 2, National Snow and Ice Data Center, Boulder, Colo. [Available at http://nsidc.org/data/docs/noaa/g02202_ice_conc_cdr/.]
- Mikaloff Fletcher, S. E., et al. (2006), Inverse estimates of anthropogenic CO₂ uptake, transport, and storage by the ocean, *Global Biogeochem. Cycles*, 20, GB2002, doi:10.1029/2005GB002530.
- Moore, J. K., and M. R. Abbott (2000), Phytoplankton chlorophyll distributions and primary production in the Southern Ocean, *J. Geophys. Res.*, 105(C12), 28,709–28,722.
- Moore, J. K., and M. R. Abbott (2002), Surface chlorophyll concentrations in relation to the Antarctic Polar Front: Seasonal and spatial patterns from satellite observations, *J. Mar. Syst.*, 37(1), 69–86.
- Moreau, S., M. Vancoppenolle, B. Delille, J.-L. Tison, J. Zhou, M. Kotovitch, D. N. Thomas, N.-X. Geilfus, and H. Goosse (2015), Drivers of inorganic carbon dynamics in first-year sea ice: A model study, *J. Geophys. Res. Oceans*, 120, 471–495, doi:10.1002/2014JC010388.
- Morrison, A. K., T. L. Frölicher, and J. L. Sarmiento (2015), Upwelling in the Southern Ocean, *Phys. Today*, 68(1), 27–32.
- Munro, D. R., N. S. Lovenduski, T. Takahashi, B. B. Stephens, T. Newberger, and C. Sweeney (2015), Recent evidence for a strengthening CO₂ sink in the Southern Ocean from carbonate system measurements in the Drake Passage (2002–2015), *Geophys. Res. Lett.*, 42, 7623–7630, doi:10.1002/2015GL065194.
- Olsen, A., et al. (2016), The global ocean data analysis project version 2 (glo dap v2)—An internally consistent data product for the world ocean, *Earth Syst. Sci. Data*, 8(2), 297–323, doi:10.5194/esd-8-297-2016.
- Park, Y.-H., J.-L. Fuda, I. Durand, N. Garabato, and C. Alberto (2008), Internal tides and vertical mixing over the Kerguelen Plateau, *Deep Sea Res., Part II*, 55(5–7), 582–593.
- Peters, W., et al. (2007), An atmospheric perspective on North American carbon dioxide exchange: CarbonTracker, *Proc. Natl. Acad. Sci. U. S. A.*, 104(48), 18,925–18,930.
- Planquette, H., et al. (2007), Dissolved iron in the vicinity of the Crozet Islands, Southern Ocean, *Deep Sea Res., Part II*, 54(18), 1999–2019.
- Resplandy, L., J. Boutin, and L. Merlivat (2014), Observed small spatial scale and seasonal variability of the CO₂ system in the Southern Ocean, *Biogeosciences*, 11(1), 75–90.
- Resplandy, L., R. Séférian, and L. Bopp (2015), Natural variability of CO₂ and O₂ fluxes: What can we learn from centuries-long climate models simulations?, *J. Geophys. Res. Oceans*, 120, 384–404, doi:10.1002/2014JC010463.
- Rosso, I., A. M. Hogg, R. Matear, and P. G. Strutton (2016), Quantifying the influence of sub-mesoscale dynamics on the supply of iron to Southern Ocean phytoplankton blooms, *Deep Sea Res., Part I*, 115, 199–209.
- Santana-Casiano, J. M., M. González-Dávila, and I. R. Ucha (2009), Carbon dioxide fluxes in the Benguela upwelling system during winter and spring: A comparison between 2005 and 2006, *Deep Sea Res., Part II*, 56(8), 533–541.
- Signorini, S. R., and C. R. McClain (2009), Effect of uncertainties in climatologic wind, ocean pCO₂, and gas transfer algorithms on the estimate of global sea-air CO₂ flux, *Global Biogeochem. Cycles*, 23, GB2025, doi:10.1029/2008GB003246.
- Takahashi, T., et al. (2002), Global sea-air CO₂ flux based on climatological surface ocean pCO₂, and seasonal biological and temperature effects, *Deep Sea Res., Part II*, 49(9), 1601–1622.
- Takahashi, T., et al. (2009), Climatological mean and decadal change in surface ocean pCO₂, and net sea-air CO₂ flux over the global oceans, *Deep Sea Res., Part II*, 56(8), 554–577.
- Takahashi, T., C. Sweeney, B. Hales, D. W. Chipman, T. Newberger, J. G. Goddard, R. A. Iannuzzi, and S. C. Sutherland (2012), The changing carbon cycle in the Southern Ocean, *Oceanography*, 25(3), 26–37.
- Talley, L., et al. (2016), Changes in ocean heat, carbon content, and ventilation: A review of the first decade of GO-SHIP global repeat hydrography, *Annu. Rev. Mar. Sci.*, 8, 185–215.

- Talley, L. D. (2008), Freshwater transport estimates and the global overturning circulation: Shallow, deep and throughflow components, *Prog. Oceanogr.*, 78(4), 257–303.
- Talley, L. D. (2013), Closure of the global overturning circulation through the Indian, Pacific, and Southern Oceans: Schematics and transports, *Oceanography*, 26(1), 80–97.
- Tamsitt, V., L. D. Talley, M. R. Mazloff, and I. Cerovečki (2016), Zonal variations in the Southern Ocean heat budget, *J. Clim.*, 29(18), 6563–6579.
- Unkovich, M. J., J. S. Pate, A. McNeill, and J. Gibbs (2013), *Stable Isotope Techniques in the Study of Biological Processes and Functioning of Ecosystems*, vol. 40, Springer, Kluwer Academic, Dordrecht, The Netherlands.
- Verdy, A., and M. R. Mazloff (2017), A data assimilating model for estimating Southern Ocean biogeochemistry, *J. Geophys. Res. Oceans*, 122, doi:10.1002/2016JC012650.
- Wanninkhof, R. (1992), Relationship between wind speed and gas exchange over the ocean, *J. Geophys. Res. Oceans*, 97(C5), 7373–7382.
- Wanninkhof, R., et al. (2013), Global ocean carbon uptake: Magnitude, variability and trends, *Biogeosciences*, 10, 1983–2000.
- Williams, N., et al. (2017), Calculating surface ocean pCO₂ from biogeochemical Argo floats equipped with pH: An uncertainty analysis, *Global Biogeochem. Cycles*, 31, 591–604.
- Williams, R. G., and M. J. Follows (2011), *Ocean Dynamics and the Carbon Cycle: Principles and Mechanisms*, Cambridge Univ. Press, Cambridge, U. K.